LAWRENCE
LIVERMORE
NATIONAL
LABORATORY

LLNL-TR-817055

CO2 injection with fracturing in geomechanically protected caprock: Final Report for Task 6 of LLNL's Research Activities to Support DOE's Carbon Storage Program (FWP-FEW0191)

P. Fu, X. Ju, J. Huang, R. R. Settgast, J. P. Morris

November 24, 2020

Disclaimer

This document was prepared as an account of work sponsored by an agency of the United States government. Neither the United States government nor Lawrence Livermore National Security, LLC, nor any of their employees makes any warranty, expressed or implied, or assumes any legal liability or responsibility for the accuracy, completeness, or usefulness of any information, apparatus, product, or process disclosed, or represents that its use would not infringe privately owned rights. Reference herein to any specific commercial product, process, or service by trade name, trademark, manufacturer, or otherwise does not necessarily constitute or imply its endorsement, recommendation, or favoring by the United States government or Lawrence Livermore National Security, LLC. The views and opinions of authors expressed herein do not necessarily state or reflect those of the United States government or Lawrence Livermore National Security, LLC, and shall not be used for advertising or product endorsement purposes.

This work performed under the auspices of the U.S. Department of Energy by Lawrence Livermore National Laboratory under Contract DE-AC52-07NA27344.

Final Technical Report:

CO_2 injection with fracturing in geomechanically protected caprock

Task 6 of LLNL's Research Activities to Support DOE's Carbon Storage Program (FWP-FEW0191)

Principal Investigator: Pengcheng Fu (fu4@llnl.gov)

LLNL Project Manager: Joshua White (white230@llnl.gov)

Technical Contributors:

Xin (Isaac) Ju, Jixiang Huang, Randolph Settgast, and Joseph Morris

Lawrence Livermore National Laboratory

November 2020

This manuscript has been authored by Lawrence Livermore National Security, LLC under Contract No. DE-AC52-07NA2 7344 with the US. Department of Energy. The United States Government retains, and the publisher, by accepting the article for publication, acknowledges that the United States Government retains a non-exclusive, paid-up, irrevocable, world-wide license to publish or reproduce the published form of this manuscript, or allow others to do so, for United States Government purposes.

Motivation

Conventional principles of the design and operation of geologic carbon storage (GCS) require injecting CO_2 below the caprock fracturing pressure to ensure the integrity of the storage complex. In non-ideal storage reservoirs with relatively low permeability, modest injection rates can lead to pressure buildup and hydraulic fracturing of the reservoir and caprock. While the GCS community has generally viewed hydraulic fractures as a key risk to storage integrity, the actual behavior of a caprock hydraulic fracture, particularly from a geomechanical perspective, has not been thoroughly studied. The prevailing method of treating a hydraulic fracture as a high-permeability wing of the storage reservoir might have resulted in erroneous understanding of caprock hydraulic fracture behavior. Comprehensive analyses of monitoring data from the In Salah project suggested that one or more hydraulic fractures may have been created in the reservoir and lower caprock system during injection operations, but did not cause detectable leakage of CO_2 out of the storage complex[1]. This observation coincides with a well-known phenomenon in the oil and gas industry: sedimentary rock formations have many inherent features that naturally protect the formations from unbounded vertical growth of hydraulic fractures.

Prior to this work, preliminary modeling work by the PI[2] has demonstrated that a vertically-contained hydraulic fracture, either in the reservoir rock or extending a limited height into the caprock, provides an effective means to access reservoir volume far from the injection well. It is therefore hypothesized that a carefully-designed stimulation treatment under appropriate geologic conditions could provide improved injectivity while maintaining overall seal integrity.

---

[1] White, J. a, Chiaramonte, L., Ezzedine, S., Foxall, W., Hao, Y., Ramirez, A., & McNab, W. (2014). Geomechanical behavior of the reservoir and caprock system at the In Salah CO2 storage project. Proceedings of the National Academy of Sciences of the United States of America, 111(24), 8747–52. https://doi.org/10.1073/pnas.1316465111

[2] Fu, P., Settgast, R. R., Hao, Y., Morris, J. P., & Ryerson, F. J. (2017). The Influence of Hydraulic Fracturing on Carbon Storage Performance. Journal of Geophysical Research: Solid Earth, 122(12), 9931–9949. https://doi.org/10.1002/2017JB014942

To quantitatively study this problem, it is necessary to develop new models that bridge the gap between (a) the over-simplified fracturing treatment in typical CO_2 reservoir models (like most existing reservoir models) and (2) the inadequate flow and transport module in existing hydraulic fracturing models (like the model in Fu et al., 2017). It is important to study mechanisms and processes contributing to the containment of hydraulic fractures as well as fracture-related phenomena unique to CO_2 injection, as opposed to the more commonly studied fracturing induced by water injection.

Proposed Research

Objective

A "geomechanically protected caprock" refers to a CO_2 storage seal with a layering structure that inherently inhibits the vertical growth of a pressure-driven fracture. In such a caprock, even if a hydraulic fracture is initiated and propagates along with injection, it is well-contained and thus the overall seal integrity is not compromised. Our ultimate objective is to study mechanisms and processes related to the containment of pressure-driven caprock fractures unique to CO_2 injection. To achieve this objective, it is necessary to develop a new fully coupled, fracture-centric simulation capability that significantly advances the state-of-the-art.

Task structure

The main heavy-listing of this project is to develop a thermo-hydro-mechanical (THM) coupled CO_2-saline two-phase hydraulic fracture model on LLNL's GEOS platform. As this new capability requires coupling many complex processes together, it has a relatively high risk. As a mitigation strategy, we first studied the sustainability of hydraulic fracture within the reservoir rock and the implication for injectivity improvement. This task requires less-challenging development work on top of existing modeling capabilities in GEOS.

Results and main findings

Results from this project have been documented in two journal manuscripts as attached. Here we briefly summarize the main findings.

The first manuscript, titled "*Thermo-poroelastic responses of a pressure-driven fracture in a carbon storage reservoir and the implications for injectivity and caprock integrity*", has been accepted for publication in *International Journal for Numerical and Analytical Methods in Geomechanics*.

The main objective was to understand: (1) under what condition a hydraulic fracture can be contained within the reservoir rock without fracturing the caprock, and (2) the process of fracture's vertical extension if fracturing in reservoir eventually leads to caprock fracturing. The underlying complexity is that even if the reservoir rock has lower in situ stress and thereby lower fracturing pressure than the caprock, reservoir is more susceptible to "back stress" induced by poromechanical effects.

We employ a high-fidelity model coupling multiphase flow, heat transport, poroelasticity, thermal contraction, as well as fracture mechanics to study thermo-poroelastic responses of a pressure-driven fracture in a carbon storage reservoir. We found that poroelasticity dictates that to maintain an open fracture in the reservoir rock requires a continuous and significant increase of pressure, potentially exceeding the fracturing pressure for the caprock. A closed-form equation is derived to conservatively compute the pressure increase. Although cooling in the near-well region could reduce the fracture-opening pressure, the fracture propagation pressure is still dictated by processes in the far-field rock unaffected by the cooling. This discrepancy causes a high net pressure near the injection well and could further drive the fracture into the caprock. However, while such fracturing is likely, we demonstrate that in many instances we can expect it to be contained.

Although the first paper already answers many questions targeted by the project, the answers are largely qualitative as the underlying model was in 2D. In the second paper, titled "*A simple method to simulate thermo-hydro-mechanical processes in leakoff-dominated hydraulic*

fracturing and the application in geological carbon storage"[3], we expand this work by developing a full 3D simulation capability and investigating more complex reservoir-caprock-fracture-fluid interaction scenarios. In this paper we developed a simple method to capture all these interplays in high fidelity by sequentially coupling a hydraulic fracturing module with a coupled thermal-hydrological-mechanical (THM) model for nonisothermal multiphase flow. The model was made numerical tractable by taking advantages of self-stabilizing features of leakoff-dominated fracturing, which was inspired by findings from the first paper. The model is validated against the PKN solution in the leakoff-dominated regime. Moreover, we employ the model to study thermo-poromechanical responses of a fluid-driven fracture in a field-scale carbon storage reservoir that is built loosely based on the In Salah project. We found many processes, including thermal, hydraulic, and mechanical processes, are involved in fracturing caused by CO_2 injection. These processes interact in convolved ways and the relative importance among these processes can evolve as injection progresses. The new model proves effective in simulating these processes and their complex interactions in fidelity that is unattainable for existing simple models. For example, thermal contraction induced by CO_2 injection has often been speculated to have a negative impact on fracture containment. Our study shows that cold fluid injection itself could actually benefit the geomechanically containment of fracturing under certain stress conditions of caprock. A gradual pumping pressure decline can be used as a practical indicator of fracture growth during injection. The proposed model proves effective in simulating practical problems on length and time scales relevant to geological carbon storage.

See the two attached manuscripts for detailed model development and practical findings.

[3] Being submitted to *International Journal of Greenhouse Gas Control*.

Appendix A: Mechanism Analysis Using a 2D Model

Published Manuscript:

Received: 10 June 2020 | Revised: 18 September 2020 | Accepted: 20 October 2020

DOI: 10.1002/nag.3165

RESEARCH ARTICLE

WILEY

Thermo-poroelastic responses of a pressure-driven fracture in a carbon storage reservoir and the implications for injectivity and caprock integrity

Pengcheng Fu[1] | **Xin Ju**[1] | **Jixiang Huang**[1] | **Randolph R. Settgast**[1] | **Fang Liu**[2] | **Joseph P. Morris**[1]

[1] Atomospheric, Earth, and Energy Division, Lawrence Livermore National Laboratory, Livermore, California, USA

[2] State Key Laboratory of Disaster Reduction in Civil Engineering, Tongji University, Shanghai, China

Correspondence
Pengcheng Fu, Atmospheric, Earth, and Energy Division, Lawrence Livermore National Laboratory, Livermore, CA 94550 USA.
Email: fu4@llnl.gov

Abstract

CO_2 injection into a reservoir with marginal permeability ($\lesssim 10^{-14}$ m^2) could induce pressure high enough to fracture the reservoir rock and/or caprock. A pressure-driven fracture can immensely enhance the injectivity and would not compromise the integrity of the overall storage complex as long as the fracture is contained vertically. Conventional models for geologic carbon storage simply treat fractures as high-permeability conduits, ignoring coupled interactions between the fluids, the fracture, the reservoir, and caprock. We employ a high-fidelity model coupling multiphase flow, heat transport, poroelasticity, thermal contraction, as well as fracture mechanics to study thermo-poroelastic responses of a pressure-driven fracture in a carbon storage reservoir. We found that poroelasticity dictates that to maintain an open fracture in the reservoir rock requires a continuous and significant increase of pressure, potentially exceeding the fracturing pressure for the caprock. A closed-form equation is derived to conservatively compute the pressure increase. Although cooling in the near-well region could reduce the fracture-opening pressure, the fracture propagation pressure is still dictated by processes in the far-field rock unaffected by the cooling. This discrepancy causes a high net pressure near the injection well and could further drive the fracture into the caprock. However, while such fracturing is likely, we demonstrate that in many instances we can expect it to be contained.

KEYWORDS

caprock integrity, geological carbon storage, hydraulic fracture, supercritical CO_2, thermo-hydro-mechanical coupling

 © 2020 John Wiley & Sons Ltd.

1. Introduction

Existing pilot and experimental geologic carbon storage (GCS) projects mostly target storage reservoirs with favorable conditions, namely high porosity, high permeability, and the presence of thick seal formations. Reservoir permeabilities in these projects are typically in the range of hundreds of mD (> 10^{-13} m^2) or even several darcies (> 10^{-12} m^2) [see Michael et al.[1] for a list]. However, to achieve the scale of GCS that could achieve substantial impact on global greenhouse gas emission[2,3], less favorable reservoirs with relatively low permeability, such as the In Salah site[4] in Algeria, the Nagaoka site in Japan[5], and the Gorgon site in Australia[6], must be considered. For many greenhouse gas source locations, there might only exist candidate reservoirs with marginal permeability within an economical distance and depth. Evaluating the conditions under which GCS can be safely deployed in such marginal reservoirs is an important research subject but has not attracted much attention.

The main challenge associated with GCS in marginal-permeability reservoirs is the low injectivity at injection pressures below typical prescribed limits. Such pressure limits are usually dictated by the fracturing pressure, that is, the pressure beyond which hydraulic fractures will emerge and propagate, either in the reservoir or caprock formations, or the pressure at which existing faults will be activated[7,8]. The likely consequence of injecting CO_2 at a typical commercial rate (~million tons per year) into a low permeability (low tens of millidarcy, mD) reservoir with a modest thickness (low tens of meters) through a vertical well has been analyzed in Fu et al.[9] By applying a "line-source" axisymmetric porous-medium flow solution[10], it was found that the injection pressure would steadily increase under a constant injection rate. After a certain amount of injection, depending on the reservoir thickness, permeability, and injection

rate, among other factors, the injection pressure could exceed the fracturing pressure of the reservoir rock, thereby creating a hydraulic fracture.

A hydraulic fracture within the reservoir formation is not a threat to the integrity of the storage system as long as the fracture does not compromise the caprock, by either vertically propagating through the caprock or conveying pressurized fluid that can activate faults/natural fractures in the caprock. In essence, hydraulic fracturing is a natural response of the rock to fluid injection: In the *porous-medium flow* (i.e. Darcy flow) regime, injection pressure increases largely linearly with the injection rate until the pressure exceeds the fracturing pressure, triggering a flow regime change. As revealed in Fu et al.[9], this new regime entails the fracture providing the contact area between the injected fluid and the reservoir volume while the growth of the fracture provides a continuously increasing contact area. The fluid pressure within the fracture only needs to be slightly higher than the minimum pressure that opens the fracture. Due to (1) the fracture's ability to grow, (2) the high compliance of an open fracture (i.e. high sensitivity of fracture aperture to pressure change)[11], and (3) the extreme sensitivity of a fracture's transmissivity to fracture aperture (i.e. the so-called "cubic law")[12], an open, propagating fracture provides practically limitless injectivity. Therefore, hydraulically fracturing the reservoir rock is a potential solution to the low injectivity problem for marginal-permeability reservoirs.

The current study intends to answer the following questions: *Can the said hydraulic fracture in a CCS reservoir be sustained with a limited injection pressure? What mechanisms could potentially drive fracture propagation into the caprock, particularly in the near-well region?* For any given CSS site, pressure higher than certain limits would cause storage integrity problems.

Such limits are usually imposed by inherent characteristics of the caprock complex, e.g., the *in situ* stress or the slipping tendency of natural fractures in the caprock[13]. The concern that the pressure needed to sustain a hydraulic fracture could increase to unsafe levels is rooted in a well-known phenomenon. Hydraulic fractures in a permeable porous medium under constant pressure tend to "close" (i.e. aperture decreases until completely close) due to the effects of poroelasticity[14]. In other words, as the pore pressure increases in the rock medium next to the fracture, which is due to the diffusion of the injected fluid into the reservoir, the effective stress decreases and the associated deformation relaxes. To keep the fracture open, the injection pressure would have to keep increasing, potentially exceeding the imposed pressure limit. Although this is a well-known phenomenon in the context of hydraulic fracturing for oil/gas reservoir stimulation[15-17], its impact on CCS reservoir could be more significant for at least three reasons. First, oil/gas reservoirs requiring fracturing stimulation usually have very low permeability and thus slow pore pressure build-up in the surrounding rock. Second, fluid injection to stimulate hydraulic fractures in oil/gas reservoirs only lasts a short period of time. Third, high-viscosity fluids are usually used as the fracturing fluid for unconventional reservoirs, which retards pressure diffusion into the rock matrix from the fracture. In contrast, even when the permeability of a carbon storage reservoir is considered marginal for CCS purposes, it is still a few orders of magnitude higher than that of unconventional oil and gas reservoirs, the injection lasts months or years, and the fracturing fluid is the super-critical CO_2 itself.

Thermal response of fractures in the storage reservoir is another important factor. The injected CO_2 is usually cooler than the reservoir rock (see a summary of reservoir temperatures in

Appendix A of Michael et al.[1]). The injection could cause significant thermal stress in the rock, thereby changing the stress state and potentially causing the propagation of fractures[18-21].

In this work, we use coupled thermo-hydro-mechanical (THM) simulations to investigate the *thermo-poroelastic responses* of a hydraulic fracture in CCS reservoir rock. Section 2 of the current paper presents the analysis framework and the underlying rationale. The formulations of the THM model, as well as a verification of the poroelastic model, are presented in Section 3. Section 4 discusses the results of 2D simulations representing the responses in an arbitrary cross-section, inspiring an analytical solution derived in section 5, which estimates the pressure required to maintain an open fracture in a porous medium. Section 6 extends the analysis to a 3D geometry and reveals how a reservoir fracture penetrates into the caprock via a thermo-mechanical effect. The practical implications of the findings are discussed in the final section.

2. Analysis framework

Analyzing thermo-poroelastic responses of a hydraulic fracture in GCS reservoirs needs to consider many complex, interconnected processes, including multi-phase multi-component flow of fluid in both the fracture and the surrounding matrix, the opening and extension of the fracture, fluid-rock-fracture heat transport, poroelastic relaxation of rock deformation, and thermal contraction of the rock. As suggested in a recent review on the modeling of caprock integrity[22], a fully coupled 3D model that can realistically capture the behaviors of CO_2-water-heat flow, rock deformation, and fracturing in a realistic geometry is not available yet. Existing models either, if rooted in multi-phase flow codes, reduces the role of a fracture to a high-permeability channel while ignoring the intricate fracture mechanics behaviors[23-25], or, if rooted

in water-based hydraulic fracturing codes, fails to faithfully capture the multi-phase flow processes[9,26,27]. It is therefore necessary to formulate the problem in a rational way to sufficiently represent critical processes while keeping the modeling tractable. The rationale behind the following analysis framework is derived from the results of Fu et al.[9]

As illustrated in Figure 1, a hydraulic fracture initiating in relatively-high permeability reservoir rock horizontally extends in the maximum horizontal *in situ* stress (S_{Hmax}) direction (along the x-axis in Figure 1) as dictated by geomechanical principles[28]. The length of the fracture (in the out-of-the plane direction) grows as the reservoir volume in contact with the fracture approaches pressure equilibrium with the fluid in the fracture, and it grows in such a rate that the accessible reservoir can accommodate the injection rate under a fracture fluid pressure that keeps the fracture open. As revealed in Fu et al.[9], the horizontal propagation of such a hydraulic fracture, either entirely contained in the reservoir rock or partly extending into the caprock, is in the so-called "leakoff-dominated" regime. The analysis in the remainder of the paper can be framed as follows:

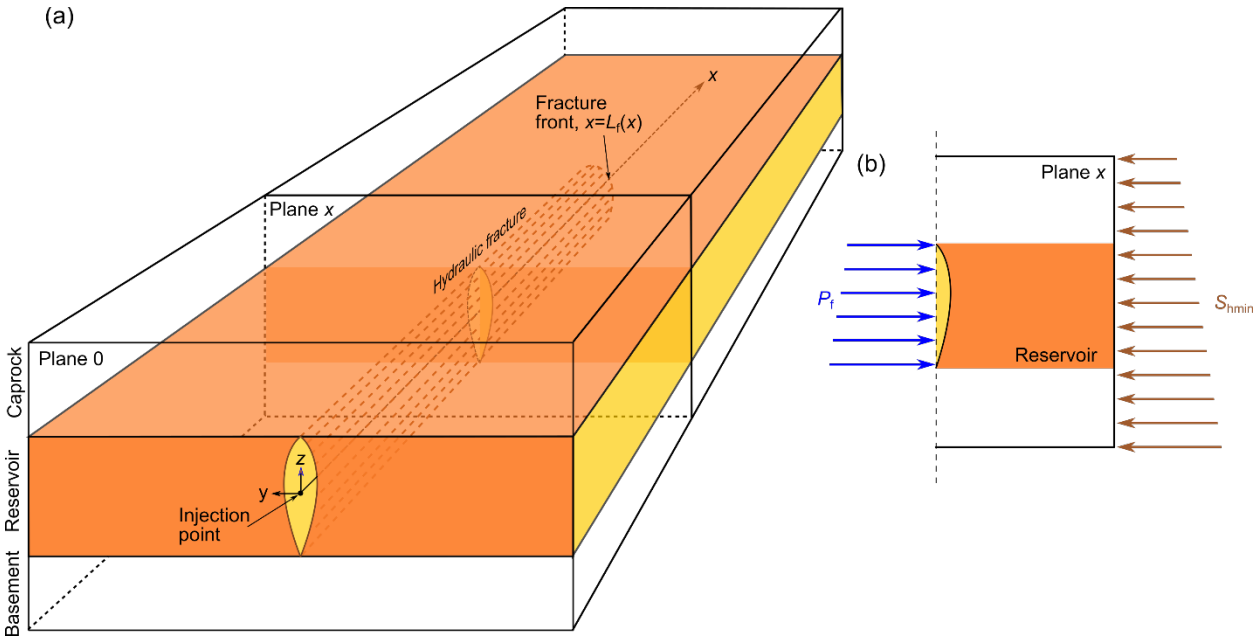

Figure 1 The configuration of rock layers around one wing of a hydraulic fracture vertically contained in the reservoir rock. The analysis in sections 4 and 5 will focus on an arbitrary cross-section in Plane x. (b) shows the fluid pressure and traction boundary conditions (both represented by P_f) applied on the fracture face as well as the distribution of S_{hmin} in the far field. Due to symmetry, a half-model with proper symmetrical boundary condition applied is sufficient.

- We focus on flow and deformation in a 2D plane, which can be seen as a cross-section perpendicular to the fracture plane at an arbitrary distance x from the injection point. This is essentially a plane-strain treatment, common in classical hydraulic fracturing models[29,30]. As the fracture aperture, fracture pressure, and reservoir saturation vary rather slowly along the fracture length, the plane-strain assumption is appropriate. For a 2D plane at an arbitrary distance x to the injection, time $t = 0$ marks the moment when the fracture front reaches this plane.
- The reservoir, caprock, and basement are represented by a continuum mesh but with different material parameters. Slipping at material interfaces is not concerned in the current study.

- On the 2D plane, the relevant "near-field" boundary conditions are (1) fluid "leaking" into the reservoir rock from the open fracture (the flow boundary) at certain pressure and temperature, and (2) pressure applied on the fracture surface (the mechanical boundary, or P_f as annotated in Figure 1(b)). The coupling between the geomechanics and the flow system is embodied by the pressures for these two boundaries being the same at any height along the fracture. Vertical flow along the fracture is minimal, so a hydrostatic condition corresponding to the density of supercritical CO_2 is applied along the fracture. The pressure at the mid-height is treated as an unknown, expected to evolve over time, and solved to satisfy the condition that the fracture needs to remain mechanically open, as detailed in section 3.4. The fluid temperature in the fracture will vary with distance from the injection point. Near the injection point, the fluid temperature on the fracture is essentially the downhole temperature of the injected fluid. At farther locations where the fluid has reached thermal equilibrium with the rock, the fracture fluid temperature would be the same as the *in situ* rock temperature.
- We apply the original reservoir pressure at the lateral boundaries as the "far-field" hydraulic boundary condition. No-flow conditions are enforced at the top and bottom surfaces. The "roller" boundary condition for the solid mechanics solver is applied to all far field boundaries.
- As the limiting pressure to secure caprock integrity is site-specific, we do not assume specific values in this generic study. Instead, we quantify the fluid pressure required to maintain an open fracture for various *in situ* conditions.
- Based on the findings from Fu et al.[9], the injection rate affects the fracture's growth speed along the *x*-axis and thereby the time when the fracture reaches a given cross-section.

However, it does not affect the loading condition and response of a given cross-section. In injection through a hydraulic fracture, a higher injection rate is accommodated by faster fracture growth, but not by more flow into each cross-section.

- Section 6 analyzes the 3D ramifications of the 2D analysis results.
- Although we do not directly address the issue of fault activation in the caprock, a hydraulic fracture extending into the caprock, as studied in the current work, could intersect and supply overpressure to faults. Therefore, this study has direct implications for the study of fault activation in the caprock.

3. Numerical methods

3.1 Multi-phase multi-component flow and heat transport model

The reservoir rock and the surrounding rocks (both caprock and basement) are treated as porous media subjected to fluid/heat flow as well as poroelastic deformation. The flow and heat transport model is based on the following assumptions and treatments, which are to a large extent similar to those in the TOUGH2-ECO2N code[31-33].

- Two components, CO_2 and water, are present in the porous media. The CO_2 component resides in the supercritical state, while the water component has gaseous (vapor) and aqueous phases.
- The storage reservoir is assumed to be initially saturated with water and the fluid injected is pure CO_2. Therefore, no air (or other gas) is present in the system.
- The fluid and thermophysical properties of CO_2 are obtained from correlations developed by Altunin et al.[34], and those of water from steam table equations given by the International Formulation Committee[35].

- Gaseous and aqueous phases are in an ideal mixture. The CO_2-water mixture system is always in chemical equilibrium. The dissolution of CO_2-water among phases (gaseous CO_2 dissolves in aqueous water; vapor distributes in gaseous CO_2) is determined by a noniterative procedure developed by Spycher et al.[36] The fluid and thermophysical properties of CO_2-water mixture system are determined by the composite values of CO_2 and water properties among individual phases, implying that the existence of water does not affect thermophysical properties of CO_2 and vice versa.
- The effects of salt in the aqueous phase are ignored. Although salinity affects the thermophysical properties of brine[37,38], particularly the dissolution of CO_2, such effects play a relatively minor role in the phenomenon concerned in our study.

Mass and energy conservation is expressed in a unified integro-differential form as

$$\frac{d}{dt}\int_{\Omega} M^{\kappa}\, d\Omega + \int_{\Gamma} \boldsymbol{F}^{\kappa}\cdot\boldsymbol{n}\, d\Gamma = \int_{\Omega} q^{\kappa}\, d\Omega,\ \ \kappa \equiv \mathrm{c}, \mathrm{w}, \theta \qquad (1)$$

which represents the mass- or the heat-balance equation when the superscript $\varkappa$ denotes a mass of pore component (i.e., CO_2 when $\varkappa = \mathrm{c}$, and water when $\varkappa = \mathrm{w}$) or heat (when $\varkappa = \theta$), respectively. Accordingly, $M^{\varkappa}$, $\boldsymbol{F}^{\varkappa}$, and $q^{\varkappa}$ are mass accumulation (or heat accumulation), fluid mass flux (or heat flow), and source or sink term of mass of component $\varkappa$ (or heat), respectively. $M^{\varkappa}$ and $\boldsymbol{F}^{\varkappa}$ are integrated over an arbitrary volume Ω bounded by a closed surface Γ with unit normal $\boldsymbol{n}$, and $\boldsymbol{F}^{\varkappa}$ is integrated over the surface Γ. Note that particle derivative, $d(\cdot)/dt$, describes the change in a field $(\cdot)$ with respect to the motion of reservoir rock. $\boldsymbol{F}^{\varkappa}$ is the fluid mass flux of component $\varkappa$ relative to reservoir rock.

For the mass-balance equation, $\kappa \equiv \mathrm{w}$ or c and the mass accumulation term is given by

$$M^{\kappa} = \sum_{J=\mathrm{A,G}} \phi S_J \rho_J X_J^{\kappa} \qquad (2)$$

where ϕ is the true porosity, defined as the ratio of the pore volume to the bulk volume in the deformed configuration; S_J (defined as the ratio of volume of phase J to pore volume) and ρ_J are the saturation and density of phase J, respectively; X_J^{κ} is the mass fraction of component $\varkappa$ in phase J. Then, the mass-fluxes term $\boldsymbol{F}^{\kappa}$ is described as

$$\boldsymbol{F}^{\kappa} = \sum_{J=\mathrm{A,G}} \boldsymbol{f}_J^{\kappa} \qquad (3)$$

where $\boldsymbol{f}_J^{\kappa}$ is the convective mass flows of component $\varkappa$ in phase J. Here we assume that the movements of mobile phases, A and G, are governed by Darcy's law due to the low fluid velocity in the porous medium. Particularly, when J ≡ A, convective mass flows $\boldsymbol{f}_{\mathrm{A}}^{\kappa}$ is given by

$$\boldsymbol{f}_{\mathrm{A}}^{\kappa} = \rho_{\mathrm{A}} X_{\mathrm{A}}^{\kappa} \boldsymbol{v}_{\mathrm{A}} \quad (4)$$

$$\boldsymbol{v}_{\mathrm{A}} = -\frac{k_{\mathrm{A}}^{\mathrm{r}}}{\mu_{\mathrm{A}}} \boldsymbol{k} (\nabla P_{\mathrm{A}} - \rho_{\mathrm{A}} \mathbf{g}) \qquad (5)$$

where $k_{\mathrm{A}}^{\mathrm{r}}$, μ_{A} and P_{A} are relative permeability, viscosity and total fluid pressure in the aqueous phase, respectively; $\boldsymbol{k}$ is the intrinsic permeability tensor. The stress dependence of permeability is not considered. ∇ is the gradient operator and **g** is the gravity vector.

When $J \equiv G$, convective $\boldsymbol{f}_{\mathrm{G}}^{\kappa}$ is given by

$$\boldsymbol{f}_{\mathrm{G}}^{\kappa} = \rho_{\mathrm{G}} X_{\mathrm{G}}^{\kappa} \boldsymbol{v}_{\mathrm{G}}, \qquad (6)$$

where $\boldsymbol{v}_{\mathrm{G}}$ is the velocity of the gaseous phase, given by

$$\boldsymbol{v}_{\mathrm{G}} = -(1 + \frac{k_{\mathrm{K}}}{P_{\mathrm{G}}}) \boldsymbol{k} \frac{k_{\mathrm{G}}^{\mathrm{r}}}{\mu_{\mathrm{G}}} (\nabla P_{\mathrm{G}} - \rho_{\mathrm{G}} \mathbf{g}), \quad (7)$$

where k_{K} is the Klinkenberg factor; $k_{\mathrm{G}}^{\mathrm{r}}$and μ_{G} are the relative permeability and viscosity in the gaseous phase, respectively; and P_{G} is the total gas pressure, i.e., the summation of partial pressures of CO_2 and water in the porous medium.

For the heat-balance equation, $\kappa = \theta$ and the heat accumulation

$$M^{\theta} = (1-\phi)\rho_{\mathrm{s}}C_{\mathrm{s}}T + \sum_{J=\mathrm{A,G}} \phi S_J \rho_J U_J, \qquad (8)$$

where ϱ_{s} and C_{s} are the density and heat capacity of the solid grains, respectively; U_J is the specific internal energy of phase J. The heat flow term $\boldsymbol{F}^{\theta}$ accounts for conduction and convection, written as

$$\boldsymbol{F}^{\theta} = -\boldsymbol{k}_{\theta}\nabla T + \sum\nolimits_{J=\mathrm{A,G}} h_J \boldsymbol{f}_J, \qquad (9)$$

where $\boldsymbol{k}_{\theta}$ denotes the composite thermal conductivity of the porous medium and h_J denotes the specific enthalpy of phase J.

The saturations of the phases occupying the pore space and mass fractions of components in phase J should each satisfy the summation condition in each control volume

$$\sum_{J=\mathrm{A,G}} S_J = 1, (11)$$

$$\sum_{\kappa=\mathrm{w,c}} X_J^{\kappa} = 1, J = \mathrm{A,G}, \qquad (12)$$

Furthermore, capillary pressure P_{C} is the difference between pressures of aqueous phase and gaseous phase, as given by

$$P_{\mathrm{C}} = P_{\mathrm{G}} - P_{\mathrm{A}}, \qquad (13)$$

For the mutual solubilities of CO_2 and water in CO_2-water mixture, we follow the approach of Spycher et al.[36], to calculate the mutual solubilities of CO_2 and water in such mixtures at chemical equilibrium.

3.2 The thermo-poroelasticity treatment

The linear-momentum balance in the porous rock matrix is expressed as

$$\nabla \cdot \boldsymbol{\sigma} + \rho_m \mathbf{g} = \mathbf{0},$$

$$\rho_m = \phi \sum\nolimits_{J=\mathrm{A,G}} S_J \rho_J + (1-\phi)\rho_{\mathrm{s}} \qquad (14)$$

Where $\nabla \cdot$ is the divergence operator, σ is the Cauchy total-stress tensor, and ρ_m is the composite matrix density. In this work, the rock matrix is assumed to be isotropic and linearly elastic.

The mass-and-energy balance equation (1) and momentum conservation equation (14) are tightly coupled by the virtue of poromechanics based on Biot and Coussy[14,39]. Here we present the mathematical formulation of thermo-poroelasticity for nonlinear multiphase fluid systems. In order to treat a multiphase porous medium as a mechanically equivalent single-phase continuum, we use the concept of equivalent pore pressure[39] to account for the total effect of fluid pressure of individual phase in a porous medium. The Cauchy total stress tensor using solid mechanic sign convention (tension is positive) in a multiphase fluid system can be expressed as:

$$\boldsymbol{\sigma} = \mathbf{C}_{dr}\colon \nabla \boldsymbol{u} - bP_{\mathrm{E}}\mathbf{1} - 3\alpha_{\mathrm{L}}K_{\mathrm{dr}}dT\mathbf{1}, \quad (15)$$

where $\mathbf{C}_{dr}$ is the drained-isothermal elastic moduli, a fourth-order elasticity tensor; $\boldsymbol{u}$ is solid displacement vector; b is the Biot coefficients; $\mathbf{1}$ is a second-order unit tensor; α_{L} is the linear coefficient of thermal expansion; K_{dr} is the drained-isothermal bulk modulus and P_{E} is the equivalent pore pressure, given by:

$$P_E = \sum_J S_J P_J - U, \quad (16)$$

where $U = \int_{S_{\mathrm{A}}}^{1} P_{\mathrm{c}}(S)\mathrm{d}S$ is the interfacial energy computed from the capillary pressure relations. Compared with other definitions of pore pressure in a multiphase porous medium, P_{E} proves to yield good numerical stability and accuracy[40]. In the deformed configuration, the differential increment in the fluid mass of phase J per unit volume of the porous medium can be rewritten as:

$$dM_J = d(\phi S_J \rho_J (1 + \varepsilon_{\mathrm{v}})), \quad (17)$$

which can be expanded as:

$$dM_J = \phi\rho_J \frac{\partial S_J}{\partial P_J} dP_J + \phi S_J \left(\frac{\partial \rho_J}{\partial P_J} dP_J + \frac{\partial \rho_J}{\partial T} dT\right) + \rho_J S_J d\phi + \phi\rho_J S_J d\varepsilon_{\mathrm{v}}, \quad (18)$$

where ε_{v} is the volumetric strain; $d\phi$ is the increment in true porosity, which can be expressed as a function of total volumetric stress, equivalent pore pressure and temperature[41]:

$$d\phi = \frac{b-\phi}{K_{\mathrm{dr}}}(dP_{\mathrm{E}} + d\sigma_{\mathrm{v}}) + 3\alpha_{\mathrm{L}} b dT, \quad (19)$$

where σ_{v} denotes volumetric total stress.

In this work, the fixed-stress iterative scheme[40] is employed to solve the two-way coupled THM problem. The scheme has been proven to be unconditionally stable and yield accurate results for coupled processes. In this scheme, the coupled problem splits into two subproblems, which are solved in a sequence. In solving the flow subproblem in each iteration, the current true porosity is estimated from its previous solution with equation (19) and assuming the rate of total volumetric stress being constant during the time step. In solving the mechanical subproblem, fluid pressures of individual phases and temperature remain fixed. Within the backward-Euler framework, the porosity change caused by the interaction between flow and geomechanics can be expressed in a discretization form:

$$\phi^{n+1} - \phi^{n} = \frac{b-\phi^{n}}{K_{\mathrm{dr}}}(P_{\mathrm{E}}^{n+1} - P_{\mathrm{E}}^{n}) + 3\alpha_{\mathrm{L}} b(T^{n+1} - T^{n}) - \Delta\phi, \quad (20)$$

$\Delta\phi$ is the porosity correction term, given as

$$\Delta\phi = \frac{-b}{K_{\mathrm{dr}}}(\sigma_{\mathrm{v}}^{n} - \sigma_{\mathrm{v}}^{n-1}), \quad (21)$$

where n - 1, n and n + 1 denote three successive points in the discretized time domain. As the processes resolved here are largely steady, convergence is usually achieved within three iterations.

3.3 Verification of the poroelastic treatment

The classical verification problem for linear poroelasticity is Terzaghi's consolidation problem[42], which describes the one-dimensional consolidation process of saturated porous media, including the generation and dissipation of overpressure. This problem is typically constrained with external loading and drainage boundary condition on both ends. The verification model is setup with a solid skeleton fully saturated with CO_2, whose parameters are listed in Table 1.

Table 1 Parameters for the verification simulation

Parameters	Values
Model length, L	40 m
Initial pore pressure, P_{int}	30 MPa
Biot's coefficient, reservoir rock, b_r	1.0
Rock intrinsic permeability, k	50 mD
Rock porosity, ϕ	0.3
Rock bulk modulus, K_{dr}	20, 200, 2000 MPa
Rock Poisson's ratio, v	0.25
Rock initial temperature, T	60°C
Rock thermal conductivity, λ	3.0 W/(m·K)
Heat capacity, C_s	1000 J/(kg·K)
Instant loading	5 MPa
CO_2 compressibility at initial pore pressure, c_f	8E-9 1/Pa
CO_2 viscosity at initial pore pressure, μ_f	7.81E-5 Pa·s

An analytical solution of Terzaghi's one-dimensional problem can be obtained by the separation of variables or Laplace transform method, in terms of the normalized pressure and dimensionless time[42,43]. The normalized pressure is defined as the ratio of current pressure to the instant

pressure induced by the external loading at the very beginning. The distance is normalized by the model's characteristic length $L/2$, half of the model length. The dimensionless time is defined as $t_{\mathrm{D}} = 4c_v t/L^2$, where c_v is the consolidation coefficient, defined as $c_v = k/\left(c_{\mathrm{r}} + \phi c_f\right)\mu_f$. This analytical solution assumes that the pore fluid is "incompressible", appropriate for the original applications where water is much less compressible than soil skeleton. For rock filled with supercritical CO_2, this assumption becomes problematic. We simulate a wide range of rock bulk moduli from 20 MPa, for which the incompressible fluid assumption remains acceptable, to 2000 MPa, representing typical reservoir rock properties.

Figure 2 compares the simulated spatial and temporal variations of pressure against analytical solutions. The model captures the development and dissipation of overpressure reasonably well. For the simulation with low modulus rock, the numerical results almost exactly match the analytical solution of the spatial variation of normalized pressure, whereas the difference is significant for the stiffer rock cases as expected.

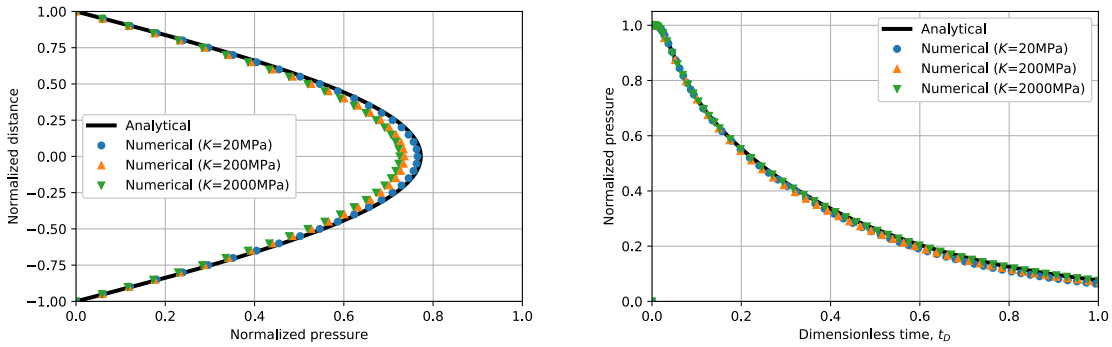

Figure 2 Comparison between three simulations of Terzaghi's one-dimensional problem with various rock bulk moduli and the analytical solution assuming incompressible pore fluid. (a) Spatial variations of normalized pressure at dimensionless time t_D = 0.1. (b) Temporal variations of normalized pore pressure at a normalized distance 0.5 (i.e. halfway between model center and boundary).

3.4 Calculating the equilibrium fracture-opening pressure

Coupling the multi-phase flow and thermo-poroelasticity alone cannot directly yield the pressure to keep the fracture open. For the plane-strain problem in Figure *1*, it is not necessary to determine the flow rate into the reservoir (i.e. the leakoff rate) per out-of-plane unit thickness to determine the state on the plane. This is because the total injection rate is the integral of the leakoff rate over the entire length of the fracture. The fracture length grows as a result of the total injection rate and the leakoff rate that each cross-section plane can accommodate. We only need to focus on the evolution of the state on the selected plane; the length growth aspect, as the consequence of in-plane state evolution, is in the "downstream" of the analysis. Therefore, for each time step, we could solve for the fracture fluid pressure that results in a target maximum aperture w_0 (i.e. the widest opening) along the fracture height. We term this pressure at the mid-depth of the reservoir layer the "equilibrium fracture pressure" as a function of w_0, $P_{\mathrm{f}}^{\mathrm{e}}(w_0)$. As shown in Fu et al.[9], for typical CO_2 injection rates, a fairly small aperture, usually a fraction of 1 mm, can provide sufficient transmissivity to conduct the injected fluid into the far field with minimal pressure loss. In the baseline model, we choose w_0=1 mm, a somewhat arbitrary small value, mainly to visualize the fracture opening geometry. When a fracture with a fixed height (H_{f}) is open, the fracture pressure linearly increases with the maximum aperture with a slope $dP_{\mathrm{f}}/dw_0 = 0.5E'/H_{\mathrm{f}}$, where E' is the plane-strain modulus. Therefore, choosing a different target aperture essentially applies a small offset on the response of the equilibrium pressure and does not affect the overall conclusion of this study. In contrast with the baseline simulation, in most models presented subsequently, we use w_0=0 as a bounding case signifying that the fracture is "barely open". The fracture pressure corresponding to w_0=0 is essentially the "fracture-opening pressure," $P_{\mathrm{f}}^{\mathrm{o}}$.

The temperature (T_{Inj}) and composition (pure supercritical CO_2) of the injected fluid are model inputs. We ignore the viscous loss caused by flow along the fracture in the vertical direction, so the fracture face is subjected to a hydrostatic gradient corresponding to the injected fluid density. To compute $P_{\mathrm{f}}^{\mathrm{e}}$ or $P_{\mathrm{f}}^{\mathrm{o}}$ in each time step, we use Newton's method and use $P_{\mathrm{f}}^{\mathrm{e}}$ or $P_{\mathrm{f}}^{\mathrm{o}}$ from the previous step as the initial guess. The derivative of w_0 with respect to injection pressure is computed numerically by adding a small perturbation to the initial guess of the pressure. The Newton method usually converges within one or two iterations.

4. Results of the baseline model.

Table 2 summarizes the computational parameters and constitutive models for the baseline simulation. The given values for reservoir S_{hmin} (total stress) and initial pore pressure P_{ini} are at the mid-depth of the reservoir layer. We assume S_{hmin} has a vertical gradient of 12 kPa/m within the storage reservoir. Because the current analysis is concerned with scenarios in which the fracture is contained in the reservoir layer, S_{hmin} in other layers of the model does not play any role in the analysis and is therefore not discussed here.

We assume the Biot coefficients of the caprock and reservoir to have relatively low values, i.e. 0.25 and 0.5. The rationale for this selection is that the hypothetical caprock-reservoir complex in our baseline model is designed to be roughly representative of the geological settings of the In Salah[4,13] where the caprock is largely dense impermeable mudstone and the reservoir is strong, moderately permeable sandstone. We use Corey-type relative permeability functions and the van Genuchten capillary function for computing relative permeability of different phases and capillary pressure, respectively. As mentioned in section 3.4, we tentatively use a target aperture

of w_0=1 mm to visualize the fracture opening geometry, although a zero aperture could be a more meaningful state. We apply the injection temperature along the fracture surface, appropriate for a cross-section near the injection well.

Table 2 Baseline simulation parameters and constitutive models for multiphase flow in porous media.

Properties	Baseline value
Reservoir thickness, H_r	20 m
Minimum principal *in situ* stress in reservoir, total stress, mid-depth, S_{hmin}	25 MPa
Initial pore pressure, mid-depth of reservoir, P_{int} (hydrostatic condition applies)	15 MPa
Biot's coefficient, reservoir rock, b_r	0.5
Biot's coefficient, caprock, b_c	0.25
Intrinsic permeability, reservoir, k_r	15 mD
Intrinsic permeability, other layers, k_c	0.1 μD
Porosity, reservoir, ϕ_r	0.15
Porosity, all other layers, ϕ_c	0.05
Young's modulus, reservoir, E_r	10 GPa
Young's modulus, other layers, E_c	30 GPa
Poisson's ratio, all layers, v	0.25
Initial temperature, all layers, T_{int}	60°C
Coefficient of thermal expansion, linear, α_L	10^{-5} /°C
Injection temperature, T_{Inj}	35°C
Thermal conductivity, all layers, λ	3.0 W/(m·K)
Heat capacity, all layers, C_s	1000 J/(kg·K)
Critical stress intensity factor (toughness), caprock	2.0 MPa·$m^{0.5}$

Relative permeability model[a] [44]	$k_{\mathrm{A}}^{\mathrm{r}} = S_{\mathrm{n}}^4$ $k_{\mathrm{G}}^{\mathrm{r}} = (1 - S_{\mathrm{n}})^2(1 - S_{\mathrm{n}}^2)$ $S_{\mathrm{n}} = (S_{\mathrm{A}} - S_{\mathrm{irA}})/(1.0 - S_{\mathrm{irA}} - S_{\mathrm{irG}})$ $S_{\mathrm{irA}} = 0.12, S_{\mathrm{irG}} = 0.01$
Capillary pressure model[b] [45]	$P_{\mathrm{C}} = -P_0[(S^*)^{-1/\lambda} - 1]^{-1/\lambda}$ $S^* = (S_{\mathrm{A}} - S_{\mathrm{irA}})/(1.0 - S_{\mathrm{irA}})$ $S_{\mathrm{irA}} = 0.11$, $P_0 = 12500$ Pa, $\lambda = 0.254$

a $k_{\mathrm{A}}^{\mathrm{r}}$ and $k_{\mathrm{G}}^{\mathrm{r}}$ are relative permeabilities in aqueous and gaseous phases, respectively defined in section 3.1; S_{n} is the normalized aqueous saturation; S_{irA} and S_{irG} are the irreducible aqueous saturation and the residual gas saturation, respectively

b P_0 is the capillary modulus

In the 2D model, rocks above and below the 20 m thick reservoir rock are represented by uniform, extensive, and elastic masses with a higher stiffness than the reservoir rock. The upper and lower boundaries are 1000 m from the reservoir (large compared with the reservoir thickness). The symmetry of the system allows the use of a half model as illustrated in Figure 1(b), and the side boundary is 2000 m (y = -2000 m) from the fracture plane. On the right-side boundary of the reservoir, Dirichlet boundary conditions are applied, matching the initial reservoir conditions. The mesh resolution is fine near the fracture, with 0.1 m in the horizontal direction and 1.0 m vertically, and progressively coarsens in the farther field, to up to 40 m in the horizontal direction.

Results of the baseline simulation are shown in Figure 3 and Figure 4. To maintain a fracture aperture of 1 mm, the fracture pressure starts from 25.6 MPa, which is slightly greater than the *in situ* total stress in the direction of opening, as expected. The equilibrium pressure experiences a rapid increase of more than 4 MPa in the first day of pressurization on this plane. As indicated by both Figure 3 and Figure 4(a), in one hour the front of significant pressure perturbation propagates much farther than the height of the fracture. The poroelastic effect causes a decrease

of effective stress (i.e. less compressive) normal to the fracture plane (Fig. 4(d)) near the fracture and a corresponding tensile strain (Fig. 4(e)) that tends to close the fracture. The equilibrium pressure is forced to increase to counteract this effect.

An interesting contrast can be observed between the horizontal effective stress increment (Fig. 4(i)) and the tensile strain increment (Fig. 4(j)) after 5 days of loading. Although the effective stress increment near the fracture is entirely tensile (red), there is a net compressive-strain zone (blue) on each side of the fracture, contributing to the opening deformation. The compression is caused by the Poisson's effect as the reservoir layer experiences vertical expansion due to the overall pressurization. After more time of injection/pressurization, the cooling zone near the fracture becomes substantial (Fig. 4(l)) and induces contraction of the rock (Fig. 4(o)). This causes a gradual reduction in the injection pressure required to maintain an open fracture as shown in Fig. 3. As the thermal front propagates slowly, this pressure decrease is also fairly slow.

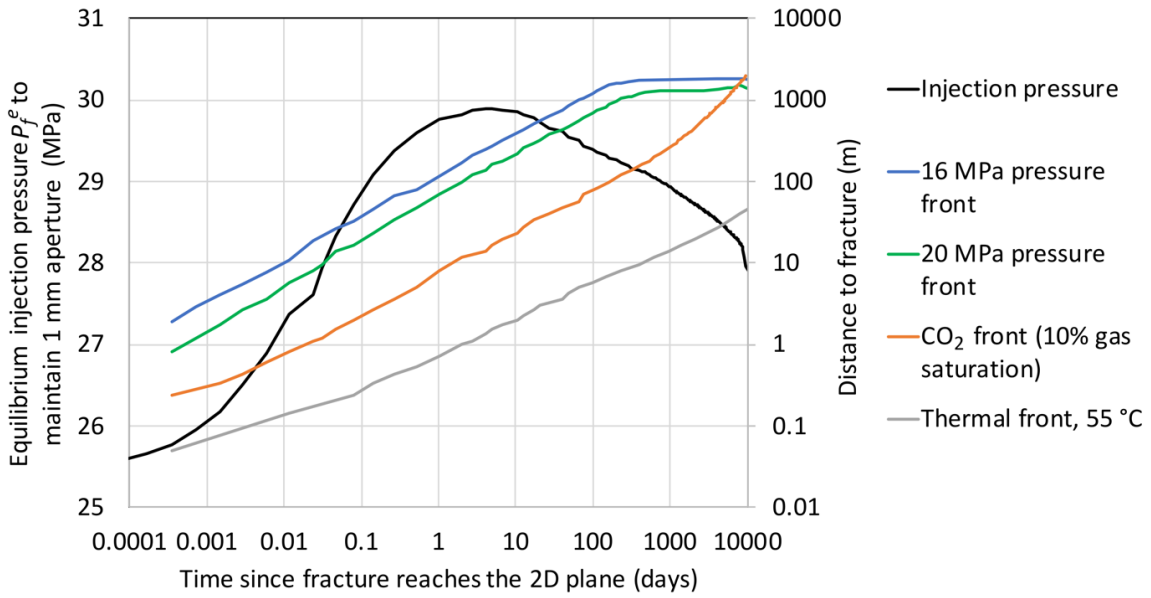

Figure 3 Results of the baseline case, showing the evolution of the pressure that keeps the fracture open with a 1 mm aperture and the horizontal propagation of pressure perturbation fronts (1 MPa and 5 MPa above the original in situ pore pressure), CO_2 front (at 10% gas saturation), and thermal perturbation front (5°C temperature decrease from the *in situ* reservoir temperature).

To qualitatively verify the roles of the Poisson's effect and thermal contraction, we simulate three idealized cases modified from the baseline case: (a) isothermal, i.e. injection fluid temperature equal to reservoir temperature, (b) zero Poisson ratio ($\nu = 0$) for the reservoir rock while Young's modulus remains the same, and (c) isothermal and $\nu = 0$. Note that case (a) also corresponds to the thermal boundary condition for a cross-section that is far from the injection well. For these cases, we obtain the fracture-opening pressure, namely the equilibrium fracture pressure corresponding to zero aperture, through simulations. We also re-simulate the baseline case targeting zero aperture instead of the 1 mm aperture in the original simulation. The comparison of the fracture pressures among the four new scenarios and the original baseline case is shown in Figure 5. In the two isothermal simulations, **Error! Reference source not found.**the fracture-opening pressure first increases like in the non-isothermal cases, but it plateaus instead of decreases in the long term. The two cases with zero Poisson's ratio require much higher

fracture-opening pressures than the cases with a typical Poisson's ratio for rocks. These observations confirm the roles played by these two factors inferred in the baseline case analysis. The difference between the original baseline case and the re-simulated case with zero aperture confirms that the arbitrarily selected aperture w_0 as postulated does not affect the varying trend of P_f^o.

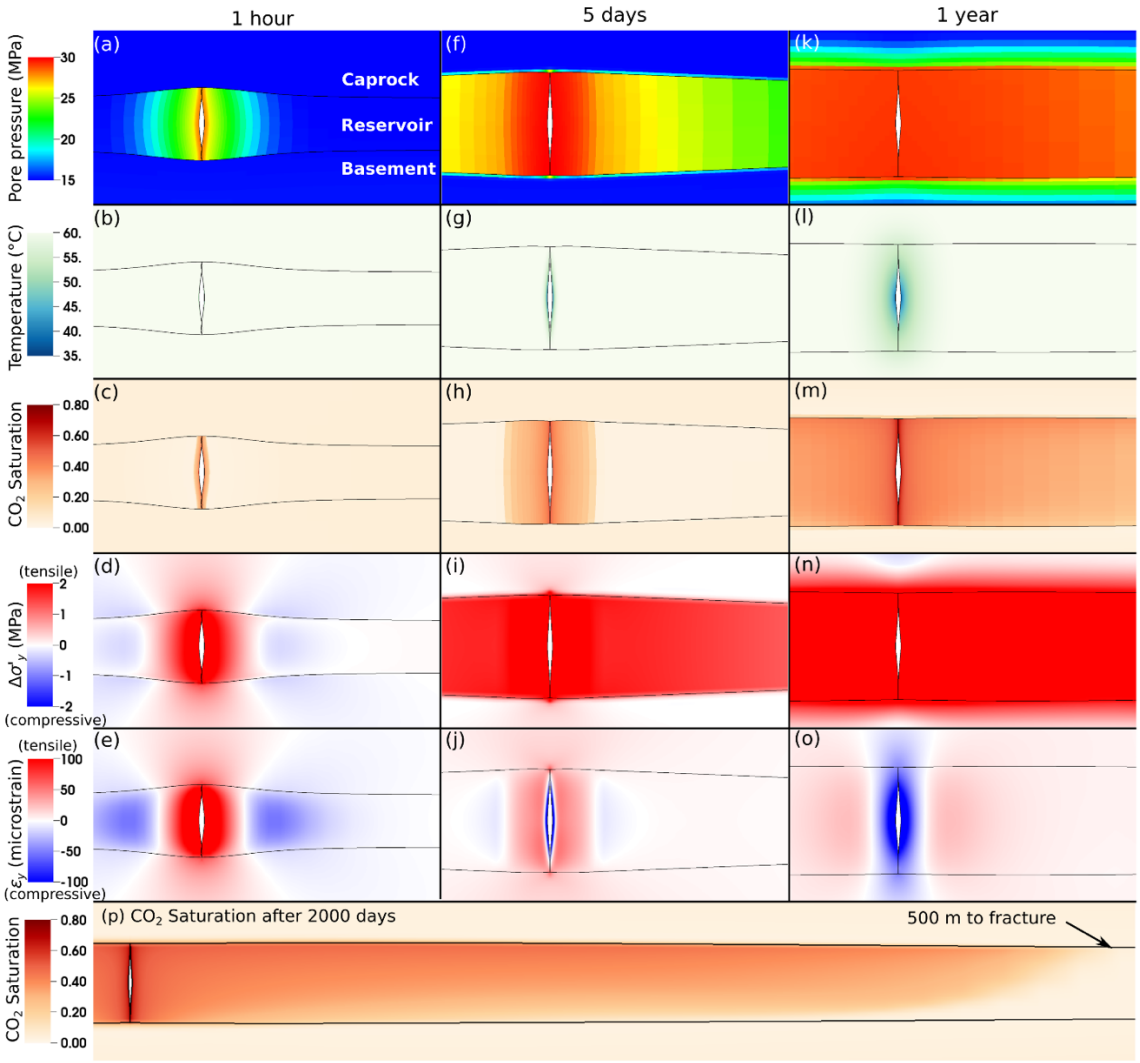

Figure 4 Selected states of the baseline simulation. Snapshots of three times for five variables near the fracture are presented in (a) through (o). (p) shows the distribution of CO_2 (critical state gas phase) in the reservoir after 2000 days of injection. The deformation is magnified by 2000 times.

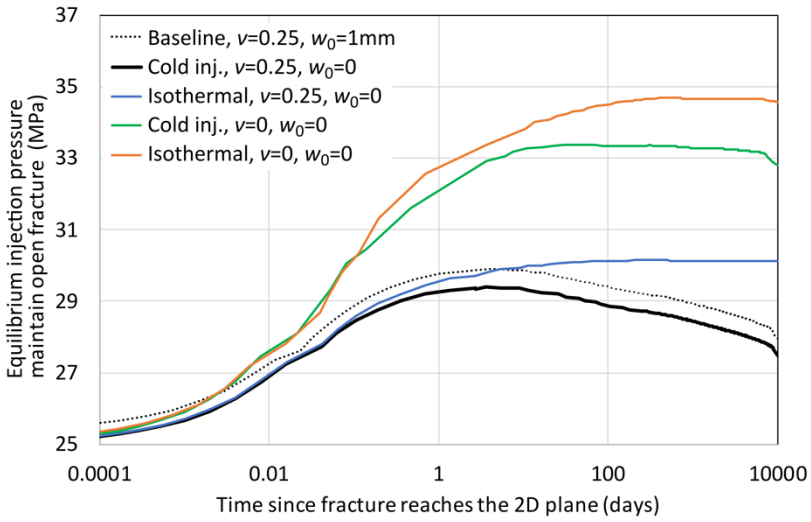

Figure 5 A comparison of the injection pressure required to keep the fracture open among four cases to illustrate the roles of the Poisson's effect and near-fracture thermal contraction. For the four cases with w_0=0, the pressure is also P_f^o.

5. An analytical solution for the upper bound of fracture-opening pressure

The long-term fracture-opening pressure $\bar{P}_f^o$ in the absence of thermal contraction, which can be considered the upper bound of the injection pressure to maintain an open fracture for any given Poisson's ratio, can be estimated in a closed-form as follows. In such a "long term" state, the reservoir pore fluid pressure has equilibrated with the fracture fluid pressure $\bar{P}_f^o$. The condition of "barely open fracture" is satisfied if the normal strain perpendicular to the fracture is zero, ε_y = 0, near the fracture in the reservoir rock. Note that the coordinate system is defined in Figure 1 and we use the original *in situ* state as the reference configuration for defining strains. Considering that the plane-strain condition in any cross-section perpendicular to the x-axis, the deformation near the fracture is essentially a laterally-constrained condition. Stress/strain increments in the two lateral directions equal to each other. For the effective stress increment, we follow the solid mechanics convention and consider tensile stress to be positive. According to Hooke's law

$$\varepsilon_y = \frac{1}{E}(\Delta\sigma'_y - \nu\Delta\sigma'_x - \nu\Delta\sigma'_z) = 0$$

In the vertical direction, the total stress should remain unchanged from the original state as it needs to balance the overburden stress.

$$\Delta\sigma_z = \Delta\sigma'_z - b(\bar{P}_{\mathrm{f}}^{\mathrm{o}} - P_{\mathrm{Ini}}) = 0$$

The balance of either of the fracture walls requires that fracture fluid pressure balances the total stress in the reservoir rock, namely

$$\bar{P}_{\mathrm{f}}^{\mathrm{o}} = b\bar{P}_{\mathrm{f}}^{\mathrm{o}} - \sigma'_{y\mathrm{i}} - \Delta\sigma'_y$$

where $\sigma'_{yi} = -S_{hmin}+bP_{Ini}$ is the initial effective stress in the reservoir rock. Solving this set of equations, we obtain

$$\bar{P}_{\mathrm{f}}^{\mathrm{o}} = P_{\mathrm{Int}} + \frac{1-\nu}{1-\nu-b+2b\nu}(S_{\mathrm{hmin}} - P_{\mathrm{Int}}) \qquad (22)$$

If we plug in the parameters in Table 1, we obtain $\bar{P}_{\mathrm{f}}^{\mathrm{o}}$=30 MPa for the baseline. If the Poisson's ratio in the baseline scenario is replaced with $\nu = 0$, we obtain $\bar{P}_{\mathrm{f}}^{\mathrm{e}}$=35 MPa. These two values are reasonably consistent with the two corresponding plateau levels (i.e. the two isothermal cases with different Poisson's ratios) in Figure 5. Note that $\varepsilon_y = 0$ in the reservoir rock surrounding the fracture is a sufficient but not a necessary condition for the fracture being barely open. It is possible that certain combinations of positive and negative ε_y around the fracture can result in the specified fracture deformation. $\varepsilon_y = 0$ is just a simple assumption to keep the problem analytically tractable. The good match between this simple formula and the numerical simulation results shows that $\varepsilon_y = 0$ is a reasonable treatment of the problem for the scenarios considered here.

Despite its simple form, this analytical solution offers many insights into the factors that affect the pressure to maintain an open fracture in CO_2 storage reservoirs. The long-term fracture-opening pressure $\bar{P}_f^o$ depends on two material parameters, b and ν, and two state variables, S_{hmin} and P_{Ini}. Both b and ν have small, finite ranges to be physically meaningful: $0<b<1$ and $0\leq\nu\leq0.5$. The factor $(1-\nu)/(1-\nu-b-2b\nu)$ as a function of b and ν is visualized in Figure 6. Its value has a fairly wide range for typical b and ν values for reservoir rocks. Note that when this coefficient equals one, $\bar{P}_f^o = S_{hmin}$. The fracture-opening pressure could be significantly greater than S_{hmin}, indicating the remarkable role of poroelasticity in determining the pressure that it takes to maintain an open fracture. A very important implication is that $\bar{P}_f^o$ for the reservoir rock could be substantially higher than S_{hmin} in the caprock. Because caprocks usually have low permeability and low Biot's coefficient, the poroelastic effect that tends to increase the fracture-opening pressure is weaker and acts slower in the caprock than in the reservoir. A practically necessary condition to prevent inadvertent caprock fracturing is that S_{hmin} of the caprock is greater than $\bar{P}_f^o$ of the reservoir. Both values only rely on in situ properties and states of the storage complex but not on operational parameters of injection.

Most other parameters do not have significant effects on the long-term fracture-opening pressure. For instance, Young's moduli of the rocks directly affect the compliance of an open fracture but have no effect on the fluid pressure at which the fracture starts to open.

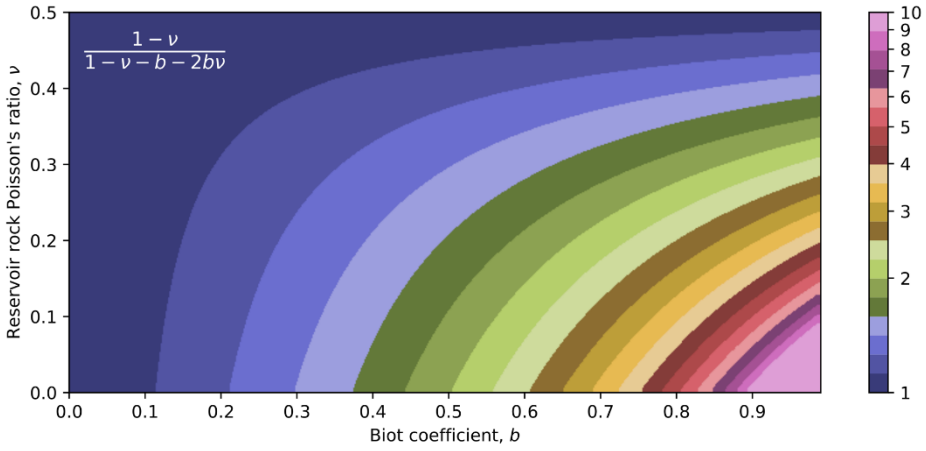

Figure 6 The coefficient in equation (22) as a function of Poisson's ratio ν and Biot's coefficient b.

6. Extending the analysis to 3D

6.1 Fracture propagation pressure

The above analyses treat a 2D plane-strain geometry that represents a *y*-*z* plane cross-section at any distance *x* from the injection source. It would be ideal to directly simulate the entire 3D domain as shown in Figure 1 using a high-fidelity model. However, mature 3D modeling capabilities that can couple CO_2-saline flow in both rock matrix and fractures with an adequate treatment of fracture mechanics are unavailable currently. The objective of the current section is to "analytically" apply the findings from the 2D analyses to a 3D scenario, in order to gain useful insights into the behavior of realistic 3D scenarios.

During active injection, each *y*-*z* cross section is in a different state depending on its distance from the injection well. With our approximation, hydraulic and mechanical loading only starts when the fracture reaches this plane. Consequently, at a given time each cross section has a different fracture-opening pressure $P_{\mathrm{f}}^{\mathrm{o}}(x,t)$. The fluid pressure along the fracture needs to both keep the entire fracture open and drive the fracture to propagate. As an open fracture has a minimal

hydraulic impedance, the fluid pressure is largely constant along the fracture (compared with gradients perpendicular to the fracture, into the matrix) and we term it the "fracture propagation pressure", P_p. If we ignore the rock's toughness, $P_p(t)=\max(P_f^o(x,t), x<L_f)$, where L_f is the length of one wing of the fracture. Note that we employ an existing fracture mechanics module in GEOS to simulate fracture propagation. The module has been verified against the analytical solutions of fracturing propagation in different regimes[47].

In section 4, we considered two scenarios in terms of the thermal boundary condition along the fracture: a non-isothermal condition where the fluid in the fracture is cooler than the rock, and an isothermal condition where the fluid has the same temperature as the rock. Although the injected fluid is typically cooler than the reservoir formation in GCS, heat exchange mostly takes place in the region near injection. In Figure 3, we observed that as the fluid flows from a fracture into the surrounding matrix, the thermal front advances much slower than the pressure perturbation front and the CO_2 front. The same applies to flow along the fracture as well, for which analytical solutions exist for some simple geometries[46]. Therefore, except for the region near the injection, the fluid should have reached thermal equilibrium with the reservoir rock before arriving at a given cross-section. Therefore, the fracture thermal boundary on a cross-section that is relatively far from the injection point resembles that of the isothermal scenario. In other words, the fracture-opening pressure for the majority of the length of the fracture is roughly the plateau level of P_f^o, as shown in the blue curve in Figure 5. This pressure is therefore also the fracture propagation pressure since P_f^o, near the wellbore, is smaller.

6.2 Modeling thermal contraction-induced fracture dilation and propagation

Due to thermal contraction in the near-wellbore region, P_f^o for small x gradually deceases and could become much smaller than the fracture propagation pressure as injection continues. This means in this region, the net pressure, namely the difference between the fluid pressure (which essentially is the fracture-propagation pressure P_p) and P_f^o, could be quite significant, resulting in large fracture aperture in this region and a strong tendency for the fracture to propagate into the caprock as illustrated in Figure 7, even when caprock's S_{hmin} is significantly greater than reservoir's fracture propagation pressure, i.e. $S_{Cap}>>P_p\approx\bar{P}_f^o$.

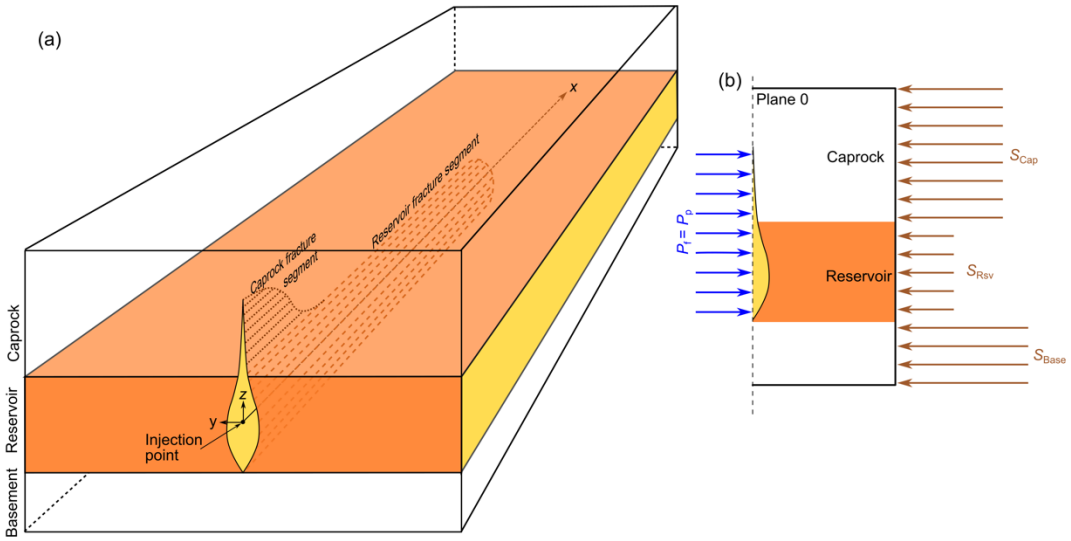

Figure 7 The 3D geometry of the hydraulic fracture near the injection penetrates into the caprock layer. (b) shows the loading condition on the cross-section at x=0. To model the extension of the fracture, a full model is needed while a half-model is shown in (b).

To illustrate this process, we perform the following simulations by modifying the baseline simulation. We only consider a y-z cross-section near the injection point, where the flowing fluid has not reached thermal equilibrium with the rock yet. Instead of seeking the fluid pressure (P_f^o) that happens to balance the evolving total stress in the reservoir rock for the current cross-section, we apply the fracture propagation pressure P_p both mechanically and hydraulically on

the fracture in the current cross-section. Based on the above analysis, P_p varies over time, and if we ignore viscous pressure loss along the open fracture, it can be approximated by P_f^o from the simulation results for the isothermal case with ν=0.25 (i.e. the blue curve in Figure 5). Note that this boundary condition also applies to the "caprock fracture", which is the part of the fracture that has extended into the caprock.

The thermal boundary condition on the caprock fracture surfaces requires additional deliberation. On the cross-section being considered, if the injected fluid flows through the caprock fracture (upper part of the fracture, flow in the out-of-plane direction) at a significant rate, the fluid temperature would be similar to the injection temperature. However, if the out-of-plane flow rate through the caprock fracture in this cross-section is low, or in other words, most of the injected fluid travels along the reservoir fracture while the caprock fracture acts like a "dead end" for flow, the fluid in the caprock fracture would be in thermal equilibrium with the caprock. The actual flow rate through the caprock fracture relative to that through the reservoir fracture is likely somewhere between the two aforementioned extreme cases. Quantitatively assessing the rate and temperature requires a full-3D coupled model which is unavailable. Therefore, we simulate the two extreme cases: the "injection temperature" or the "$T_{CapF} = T_{Inj}$" scenario, in which the injection temperature T_{Inj} is applied on the caprock fracture faces as the thermal boundary condition, and the "formation temperature" scenario or the "$T_{CapF} = T_{Cap}$" scenario, which applies the original caprock formation temperature T_{Cap} on caprock fracture. Note that for both cases, the injection temperature is applied on the reservoir fracture.

The stress intensity factor (SIF) at the fracture tip is computed using a Modified Virtual Crack Closure Technique (MVCCT[47]) which had been extensively verified to be accurate for conditions involving inter-layer stress and/or stiffness contrasts[48]. When SIF becomes greater than the toughness (also known as the critical SIF, assumed here to be a typical value of 2.0 MPa·m$^{0.5}$) of the rock containing the fracture tip, the fracture propagates. The properties and *in situ* states of the rock layers are the same as those for the baseline case, except that S_{hmin} is a constant for each layer. We consider four levels of S_{hmin} in the caprock, S_{Cap}=32, 34, 36, and 38 MPa, as a sensitivity parameter. Note that caprock S_{Cap} lower than 30 MPa would result in uncontained fracture growth even without thermal contraction. Such scenarios are therefore considered inherently unacceptable and not considered for further simulation and analysis. We assume that there is a hard fracture barrier between the reservoir and the basement, so downward fracturing is not considered.

6.3 Simulation results

Eight simulations, with four levels of caprock *in situ* stresses (S_{Cap} = 32, 34, 36, and 38 MPa), each with two kinds of thermal boundary conditions on the caprock fracture ($T_{CapF} = T_{Inj}$ and $T_{CapF} = T_{Cap}$) are performed. In all cases, the fracture grows into the caprock layer. The growth of the penetration depth is shown in Figure 8, and the fracture aperture, pore pressure, and temperature distributions in selected cases are shown in Figure 9. In three simulations, including both thermal boundary conditions for S_{Cap} = 32 MPa, and the $T_{CapF} = T_{Inj}$ scenario for S_{Cap} = 34 MPa, the fracture penetrated through the first 100 m of the caprock, which is discretized with high-resolution mesh, within one year or sooner. Since the fracture fluid pressure in all these cases is lower than the original *in situ* stress in the caprock, the sustained fracture growth is mainly

driven by the thermal contraction, which in effect reduces the *in situ* total stress in the rock. Particularly for the two cases with $T_{CapF} = T_{Inj}$, the cooling front advances along with the fracture, and the fracture propagation is analogous to a "thermal erosion". For the scenarios with $S_{Cap} = 34$ MPa with $T_{CapF} = T_{Cap}$ and $S_{Cap} = 36$ MPa with $T_{CapF} = T_{Inj}$, the caprock fractures are eventually contained, but the penetration depths are still several times larger than the original reservoir layer thickness. For the very high stress scenarios with $S_{Cap} = 38$ MPa, the fractures have limited height growth. It is interesting to note that despite the slow growth rate, the fracture continues to grow under $T_{CapF} = T_{Inj}$ throughout the entire simulation, indicating "thermal erosion" still takes place even for high *in situ* stress levels.

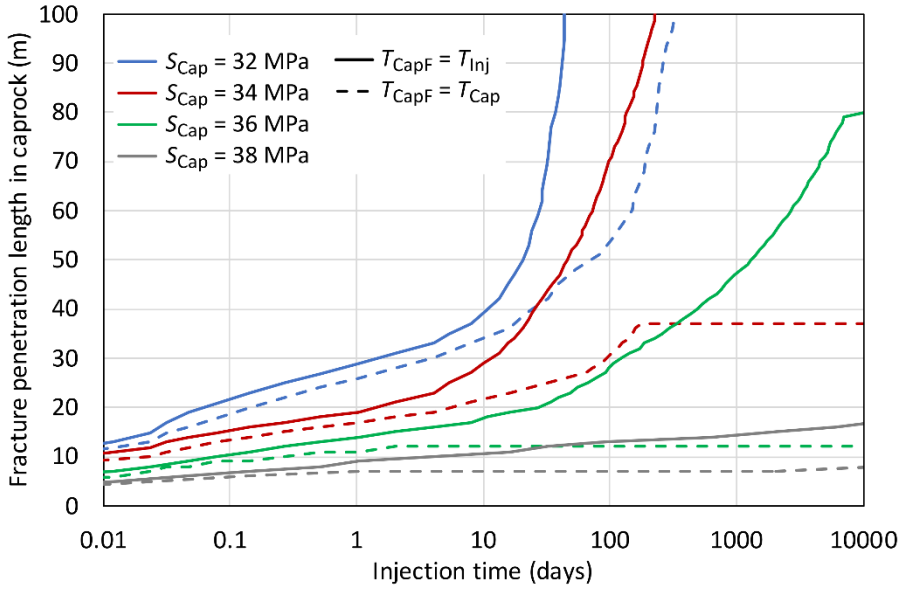

Figure 8 The penetration length of the reservoir rock fracture into the caprock near the injection due to a combined effect of fluid pressure and the rock's thermal contraction.

It is important to point out that the plane-strain assumption is likely to have caused overestimations of the fracture's penetration depth into the caprock, making these conservative estimations. As illustrated schematically in Figure 7, the fracture only penetrates into the caprock near the injection well because the thermal front can only propagate a limited distance along the

fracture. The plane-strain assumption is only appropriate when the fracture's vertical penetration depth is much shorter than the caprock fracture's extension in the *x*-direction. Therefore, despite the many insights from the simple model, a fully coupled 3D model is still required to provide a more accurate assessment of the growth of the fracture in the caprock.

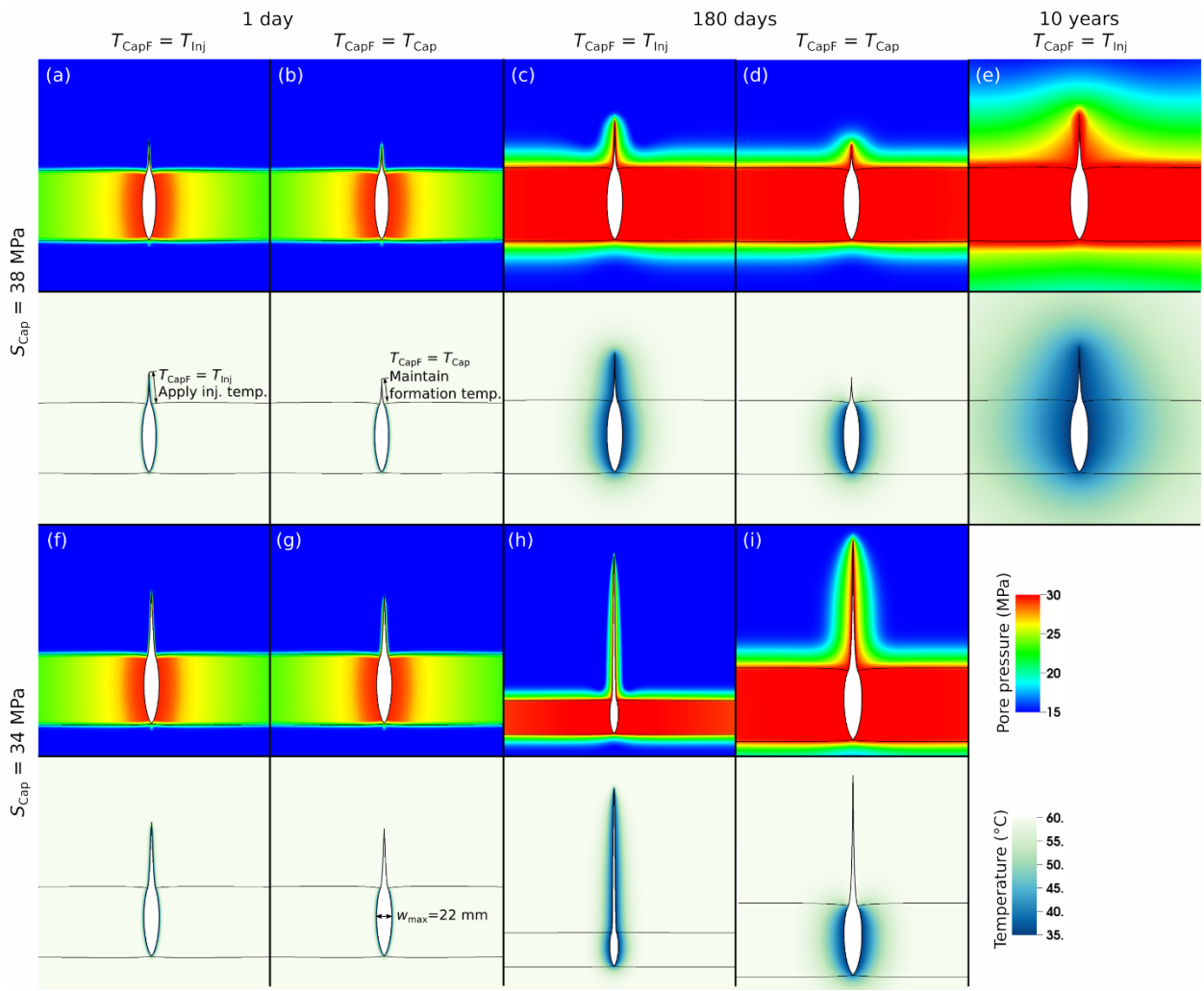

Figure 9 The states of pore pressure and rock temperature around the fracture penetrating into the caprock from the reservoir. Snapshots of two caprock *in situ* stress levels, two thermal boundaries on the caprock fracture, and three times are presented. Note that all plots have the same scales except that (h) uses a larger scale to show the entire height of the fracture, which penetrated rather deep into the caprock. The deformation is magnified by 200 times.

7. Conclusions

In this work we study the responses of a pressure-driven fracture to CO_2 injection in a geologic carbon storage (GCS) reservoir with marginal permeability. It is known that a hydraulic fracture in porous media tends to close as matrix pressure diffusion reduces the effective stress induced by the pressurization. To maintain an open fracture, and maintain injectivity, requires increasing the fracture pressure. Our main focus is to study the factors affecting such an increase in fracture-opening pressure and the implications for injectivity and caprock integrity. A two-way coupled model simulating the interactions among multi-phase flow, poroelasticity, thermal deformation, and fracture mechanics is developed and employed as the main research tool. We discovered that in addition to poroelasticity, the Poisson effect and thermal contraction also have significant effects on the evolution of the fracture-opening pressure. The simulation results inspired a closed-form solution to calculate the long-term fracture-opening pressure in the reservoir rock. For typical reservoir rock properties, this pressure can be many MPa higher than the original minimum principal stress in the reservoir rock, posing a significant risk of fracturing the caprock.

The role of thermal processes in determining the fracture-opening pressure proves to be convoluted. The injected supercritical CO_2 is typically cooler than the reservoir rock. Cooling of the rock near the fracture, which is a much slower process than pressure diffusion, tends to reduce the fracture-opening pressure. However, this only affects the region near the injection well as the thermal front does not travel the full fracture length as the fluid approaches thermal equilibrium with the surrounding rock with distance from the well. The fracture propagation pressure is therefore still dictated by the fracture-opening pressure in the region that is unaffected

by thermal stress. Near the injection well, the reduction in total stress due to thermal contraction results in higher net pressure, larger aperture, and a strong tendency for the fracture to penetrate into caprock. Moreover, if the caprock fracture carries a significant flow rate of cold fluid, the further cooling of the caprock fracture could drive the fracture to continue to propagate into the caprock (analogous to thermal erosion).

The current study indicates that pressures required to maintain an open fracture in the reservoir rock will likely cause the fracture to penetrate into the caprock. A direct implication is that to enhance injectivity in the reservoir through fracturing, the fracturing necessarily extend into the caprock to some degree. Therefore, a critical consideration for caprock integrity is to evaluate whether the caprock system itself has inherent characteristics, such as layered fabrics[49] and "rough" in situ stress profiles[50], that effectively limit fracture's height growth.

The conclusion that it is difficult to sustain a hydraulic fracture in a reservoir rock is similar to the argument in Fu et al.[9], which was based on a simplified model. However, the current more rigorous analysis employing a high-fidelity model enabled a deeper understanding of the issue and greatly improved the reliability of the conclusion. For example, the high-fidelity model revealed that a simple, widely used criterion[9,51], which states that fracturing takes place when fluid pressure is higher than the minimum principal *in situ* stress, might be problematic for CO_2 storage applications. This is because the injection itself could significantly alter the rock stress in a complex manner. The setups of the 2D models in the current study were based on findings from the 3D modeling, which used a simplified treatment of fluid flow and did not consider thermal stresses, in Fu et al.[9] A full-3D high-fidelity model is still desired to handle more complex scenarios. Our work in this direction will be reported in the near future.

References:

1. Michael K, Golab A, Shulakova V, Ennis-King J, Allinson G, Sharma S, Aiken T. Geological storage of CO2 in saline aquifers-A review of the experience from existing storage operations. *Int J Greenh Gas Control* 2010;4:659–667.
2. Pacala S, Socolow, R. Stabilization Wedges: Solving the Climate Problem for the Next 50 Years with Current Technologies. *Science* 2004; 305:968–972. DOI: 10.1126/science.1100103
3. International Energy Agency. Energy Technology Perspectives 2010: Scenarios and Strategies to 2050; 2010; International Energy Agency, Paris, France.
4. Rutqvist J, Vasco DW, Myer L. Coupled reservoir-geomechanical analysis of CO2 injection and ground deformations at In Salah, Algeria. *Int J Greenh Gas Control* 2010; 4: 225–230. DOI: 10.1016/j.ijggc.2009.10.017
5. Mito S, Xue Z, Ohsumi T. Case study of geochemical reactions at the Nagaoka CO2 injection site, Japan. *Int J Greenh Gas Control* 2008; 2, 309–318. DOI: 10.1016/j.ijggc.2008.04.007
6. Flett M, Gurton R, Weir G. Heterogeneous saline formations for carbon dioxide disposal: Impact of varying heterogeneity on containment and trapping. *J Pet Sci Eng* 2007;57: 106–118. DOI: 10.1016/j.petrol.2006.08.016
7. Zhou Q, Birkholzer JT. On scale and magnitude of pressure build-up induced by large-scale geologic storage of CO_2. *Greenh Gases Sci Technol* 2011;1: 11–20. DOI: 10.1002/ghg3.1
8. Zoback MD, Gorelick SM. Earthquake triggering and large-scale geologic storage of carbon dioxide. *Proc Natl Acad Sci USA* 2012;109: 10164–8. DOI: 10.1073/pnas.1202473109
9. Fu P, Settgast RR, Hao Y, Morris JP, Ryerson FJ. The Influence of Hydraulic Fracturing on Carbon Storage Performance. *J Geophys Res Solid Earth* 2017;122: 9931–9949. https://doi.org/10.1002/2017JB014942
10. Zimmerman RW. The Imperial College Lectures in Petroleum Engineering Volume 5: Fluid Flow in Porous Media. World Scientific; 2018.

11. Sneddon I, Elliott H. The opening of a griffith crack under internal pressure. *Q Appl Math* 1946;4: 262–267.
12. Witherspoon PA, Wang JSY, Iwai K, Gale JE. Validity of Cubic Law for fluid flow in a deformable rock fracture. *Water Resour. Res* 1980;16: 1016–1024. DOI: 10.1029/WR016i006p01016
13. Rinaldi AP, Rutqvist J. Modeling of deep fracture zone opening and transient ground surface uplift at KB-502 CO2 injection well, In Salah, Algeria. *Int J Greenh Gas Control* 2013;12: 155–167. DOI: 10.1016/j.ijggc.2012.10.017
14. Biot MA. General Theory of Three-Dimensional Consolidation. *J Appl Phys* 1941;12: 155–164. DOI: 10.1063/1.1712886
15. Detournay E, Cheng AHD, McLennan JD. A Poroelastic PKN Hydraulic Fracture Model Based on an Explicit Moving Mesh Algorithm. *J Energy Resour Technol* 1941;112: 224. DOI: 10.1115/1.2905762
16. Detournay E, Cheng AHD. Plane strain analysis of a stationary hydraulic fracture in a poroelastic medium. *Int J Solids Struct* 1991;27: 1645–1662. DOI: 10.1016/0020-7683(91)90067-P
17. Salimzadeh S, Paluszny A, Zimmerman RW. Three-dimensional poroelastic effects during hydraulic fracturing in permeable rocks. *Int J Solids Struct* 2016;0: 1–11. DOI: 10.1016/j.ijsolstr.2016.12.008
18. Preisig M, Prévost JH. Coupled multi-phase thermo-poromechanical effects. Case study: CO2 injection at In Salah, Algeria. *Int J Greenh Gas Control* 2011;5: 1055–1064. DOI: 10.1016/j.ijggc.2010.12.006
19. Gor GY, Elliot TR, Prévost JH. Effects of thermal stresses on caprock integrity during CO2 storage. *Int J Greenh Gas Control* 2013;12: 300–309. DOI: 10.1016/j.ijggc.2012.11.020
20. Vilarrasa V, Rinaldi AP, Rutqvist J. Long-term thermal effects on injectivity evolution during CO2 storage. *Int J Greenh Gas Control* 2017;64: 314–322. DOI: 10.1016/j.ijggc.2017.07.019
21. Vilarrasa V, Rutqvist J. Thermal effects on geologic carbon storage. *Earth Sci Rev* 2017;165: 245–256. DOI: 10.1016/j.earscirev.2016.12.011
22. Paluszny A, Graham CC, Daniels KA, Tsaparli V, Xenias D, Salimzadeh S, Whitmarsh L, Harrington JF, Zimmerman RW. Caprock integrity and public perception studies of carbon

storage in depleted hydrocarbon reservoirs. *Int J Greenh Gas Control* 2020;98: 103057. DOI:10.1016/j.ijggc.2020.103057

23. Morris JP, Hao Y, Foxall W, McNab W. A study of injection-induced mechanical deformation at the In Salah CO2 storage project. *Int J Greenh Gas Control* 2011;5: 270–280. DOI: 10.1016/j.ijggc.2010.10.004
24. Rinaldi AP, Rutqvist J. Modeling of deep fracture zone opening and transient ground surface uplift at KB-502 CO2 injection well, In Salah, Algeria. *Int J Greenh Gas Control* 2013;12: 155–167. DOI: 10.1016/j.ijggc.2012.10.017
25. Huang ZQ, Winterfeld PH, Xiong Y, Wu YS, Yao J. Parallel simulation of fully-coupled thermal-hydro-mechanical processes in CO_2 leakage through fluid-driven fracture zones. *Int J Greenh Gas Control* 2015;34: 39–51. DOI: 10.1016/j.ijggc.2014.12.012
26. Gheibi S, Vilarrasa V, Holt RM. Numerical analysis of mixed-mode rupture propagation of faults in reservoir-caprock system in CO2 storage. *Int J Greenh Gas Control* 2018:71; 46–61. DOI: 10.1016/j.ijggc.2018.01.004
27. Salimzadeh S, Paluszny A, Zimmerman RW. Effect of cold CO2 injection on fracture apertures and growth. *Int J Greenh Gas Control* 2018;74: 130-141. DOI: 10.1016/j.ijggc.2018.04.013
28. Hubbert KM, Willis DG. Mechanics of Hydraulic Fracturing. *Trans Am Inst Min Metall Eng* 1957;210: 153–163.
29. Nordgren RP. Propagation of a Vertical Hydraulic Fracture. *Soc Pet Eng J* 1972;12: 306–314. DOI: 10.2118/3009-PA
30. Adachi J, Siebrits E, Peirce A, Desroches J. Computer simulation of hydraulic fractures. Int. *J Rock Mech Min Sci* 2007;44: 739–757. DOI: 10.1016/j.ijrmms.2006.11.006
31. Pruess K, Oldenburg C, Moridis G. TOUGH2 User's Guide, Version 2.0. Report LBNL-43134; 1999; Lawrence Berkeley National Laboratory, Berkeley, CA.
32. Pruess K. The TOUGH codes-a family of simulation tools for multiphase flow and transport processes in permeable media. *Vadose Zo J* 2004;3: 738–746. DOI: 10.2113/3.3.738
33. Pruess K. ECO2N: A TOUGH2 fluid property module for mixtures of water, NaCl, and CO2. Technical report of Lawrence Berkeley National Laboratory (LBNL-57952); 2005; Berkeley, CA. DOI: 10.2172/877331

34. Altunin VV. Thermophysical properties of carbon dioxide (in Russian). Moscow: Publishing House of Standards; 1975.
35. International Formulation Committee (IFC) of the 6th International Conference on the Properties of Steam, The 1967 IFC Formulation for Industrial Use, Verein Deutscher Ingenieure, Düsseldorf, 1967.
36. Spycher N, Pruess K, Ennis-King J. CO2–H2O mixtures in the geological sequestration of CO2: I. Assessment and calculation of mutual solubilities from 12 to 100 ◦C and up to 600 bar. *Geochimica et Cosmochimica Acta* 2003;67: 3015–3031.
37. Silvester LF, Pitzer KS. Thermodynamics of geothermal brines. I. Thermodynamic properties of vapor-saturated NaCl (aq) solutions from 0–300 °C; 1976; Lawrence Berkeley National Laboratory, Berkeley, CA, Rep LBL-4456.
38. Duan ZH, Sun R. An improved model calculating CO2 solubility in pure water and aqueous NaCl solutions from 273 to 533K and from 0 to 2000 bar. *Chemical Geology* 2003;193: 257–271.
39. Coussy O. Poromechanics. Wiley; 2004.
40. Kim J, Tchelepi HA, Juanes R. Stability and convergence of sequential methods for coupled flow and geomechanics: Fixed-stress and fixed-strain splits. *Comput Methods Appl Mech* Eng 2011;200: 1591–1606. DOI: 10.1016/j.cma.2010.12.022
41. Kim J, Sonnenthal EL, Rutqvist J. Formulation and sequential numerical algorithms of coupled fluid/heat flow and geomechanics for multiple porosity materials. *Int J Numer Methods Eng* 2012;92(5): 425-456.
42. Terzaghi K. Theoretical Soil Mechanics. New York: John Wiley & Sons; 1943.
43. Verruijt A. Computational Geomechanics. Kluwer Academic Publishers: Dordrecht; 1995.
44. Brooks RH, Corey AT. Properties of porous media affecting fluid flow. American Society of Civil Engineers Proceedings, Journal of the Irrigation and Drainage Division 1966; 92(IR2):61–88.
45. Van Genuchten MT. A closed form equation for predicting the hydraulic conductivity of unsaturated soils. *Soil Sci Soc Am J* 1980;44: 892–898.
46. Gringarten AC, Witherspoon PA, Ohnishi Y. Theory of heat extraction from fractured hot dry rock. *J Geophys Res* 1975;80: 1120–1124. DOI: 10.1029/jb080i008p01120

47. Settgast RR, Fu P, Walsh SDC, White JA, Annavarapu C, Ryerson FJ. A fully coupled method for massively parallel simulation of hydraulically driven fractures in 3-dimensions. *Int J Numer Anal Methods Geomech* 2017;41: 627–653. DOI: 10.1002/nag.2557
48. Huang J, Fu P, Settgast RR, Morris JP, Ryerson FJ. Evaluating a Simple Fracturing Criterion for a Hydraulic Fracture Crossing Stress and Stiffness Contrasts. *Rock Mech. Rock Eng* 2019;52: 1657–1670. DOI: 10.1007/s00603-018-1679-7
49. Fisher MK, Warpinski NR. Hydraulic-Fracture-Height Growth: Real Data. *SPE Prod Oper* 2012;27: 8–19. DOI: 10.2118/145949-PA
50. Fu P, Huang J, Settgast RR, Morris JP, Ryerson FJ. Apparent Toughness Anisotropy Induced by Roughness of In-Situ Stress: A Mechanism That Hinders Vertical Growth of Hydraulic Fractures and Its Simplified Modeling. *SPE J* 2019;24: 2148–2162. DOI: 10.2118/194359-PA
51. Mathias SA, Hardisty PE, Trudell MR, Zimmerman RW. Approximate solutions for pressure buildup during CO2 injection in brine aquifers. *Transp Porous Media* 2009;79: 265–284. DOI: 10.1007/s11242-008-9316-7

Manuscript in review:

A simple method to simulate thermo-hydro-mechanical processes in leakoff-dominated hydraulic fracturing and the application in geological carbon storage

Xin Ju, Pengcheng Fu*, Randolph Settegast, Joseph Morris

Atomospheric, Earth, and Energy Division, Lawrence Livermore National Laboratory, Livermore, CA 94550 USA.

*Corresponding author: fu4@llnl.gov

Abstract: A potential risk of injecting CO_2 into storage reservoirs with marginal permeability ($\lesssim 10^{-14}$ m^2) is that commercial injection rates could induce fracturing of the reservoir and/or the caprock. Such fracturing is essentially fluid-driven fracturing in the leakoff-dominated regime. Recent studies, suggested that fracturing, if contained within the lower portion of the caprock comples, could substantially improve the injectivity without compromising the overall seal integrity. Modeling this phenomenon entails complex coupled interactions among the fluids, the fracture, the reservoir, and the caprock. We develop a simple method to capture all these interplays in high fidelity by sequentially coupling a hydraulic fracturing module with a coupled thermal-hydrological-mechanical (THM) model for nonisothermal multiphase flow. The model was made numerical tractable by taking advantages of self-stabilizing features of leakoff-dominated fracturing. The model is validated against the PKN solution in the leakoff-dominated regime. Moreover, we employ the model to study thermo-poromechanical responses of a fluid-driven fracture in a field-scale carbon storage reservoir that is built loosely based on the In Salah project. The model reveals complex yet intriguing behaviors of the reservoir-caprock-fluid system with fracturing induced by cold CO_2 injection. We also study the effects of the *in situ* stress contrast between the reservoir and caprock and thermal contraction on the vertical

containment of the fracture. The proposed model proves effective in simulating practical problems on length and time scales relevant to geological carbon storage.

1 Introduction

Geological carbon storage (GCS) is a promising measure to mitigate the effect of anthropogenic greenhouse gas emissions on climate change (Pacala and Socolow, 2004; International Energy Agency, 2010). To have a meaningful impact on the net CO_2 emission through GCS requires injecting a large quantity of CO_2 into subsurface geological reservoirs (Orr, 2009; Haszeldine, 2009). Existing pilot and experimental GCS projects mainly focus on storage reservoirs with ideal conditions, such as high porosity and high permeability (typically in the range of hundreds to thousands of millidarcy (1 mD = 10^{-15} m^2)). Considering that high quality reservoirs do not necessarily exist near CO_2 sources, the utilization of less favorable reservoirs, such as those with marginal permeabilities (i.e. low tens of mD), can significantly improve the commercial viability of CGS. In particular, recent commercial-scale field tests demonstrate that many such low permeability reservoirs have enormous CO_2 sources nearby and also enjoy easy access to drilling and comprehensive monitoring systems (Mito et al., 2008, Rinaldi et al, 2013). One good example of such sites is in the In Salah, Algeria, where a large amount of CO_2 source from nearby natural gas production was injected into several storage reservoirs with marginal permeabilities (around 10 mD) (Iding and Ringrose, 2010; Rinaldi et al., 2013). Therefore, understanding CGS in reservoirs with marginal permeability is of great significance.

The main challenge facing injection into marginal-permeability reservoirs is the low injectivity under the pressure constraints that prevent fluid-driven fractures, namely, hydraulic fractures, from occurring in storage reservoirs. Previous studies showed that using a low injection rate that complies with the pressure constraint cannot achieve even a moderate commercial-level injection rate, i.e. a million-metric ton per year (Fu et al., 2017). However, recent studies postulated that the issue of low injectivity in marginal-permeability reservoirs might be effectively and safely mitigated if injection-triggered hydraulic fractures can be contained within reservoir rocks or the lower portion of the caprock without jeopardizing the overall seal integrity of the caprock

complex (White et al., 2014; Fu et al., 2017). Circumstantial field data and observations from the In Salah site also suggest the possible existence of such postulated scenarios (Bohloli et al., 2017; Oye et al., 2013; White et al., 2014).

Modeling hydraulic fracturing in marginal-permeability GCS reservoirs entails the simulation of many complex processes: multiphase multicomponent fluid flow and heat transfer within fractures and matrix, mass and heat exchanges between fracture and matrix flows, poro/thermo-elastic deformation of solid rocks, and fracture propagation. Although many numerical studies have tackled this challenging task, significant simplifications had been made to mitigate various numerical challenges. These simplifications could be broadly divided into two groups: (1) treating hydraulic fractures as a highly permeable porous zone and (2) simplifying multiphase and nonisothermal flow behaviors of injected CO_2.

The first group of works typically simplify the dynamic interactions between fracture propagation and matrix flows and also neglect some key characteristics of hydraulic fractures (e.g. Morris et al., 2011; Pan et al., 2012; Raziperchikolaee et al., 2013; Sun et al., 2016). In other words, these are not designed to accurately predict the coupled thermo-hydro-mechanical (THM) responses of reservoir and caprocks once fluid-driven fractures are created. Many models in this category employ a continuum-based method, such as the dual porosity models and dual permeability models (e.g. Guo et al., 2017; Li and Elsworth 2019; Fan et al., 2019), neither of which could represent the complex flow behaviors associated with a propagating fracture. Moreover, works that attempt to capture geomechanical responses of hydraulic fractures often do not address complexities caused by an evolving fracture tip (e.g. Gor et al. 2014; Eshiet and Sheng 2014; Vilarrasa et al., 2014). In other words, they cannot explicitly depict the evolution of fracture extents and shapes which is critical to evaluating fracture containment (Rutqvist et al., 2016; Ren et al., 2017; Vilarrasa et al., 2017; Sun et al., 2017).

The second group of works, on the other hand, strive to capture essential features associated with hydraulic fracturing, such as fracturing propagation, seepage (leakoff) of fluid through fractures

into reservoirs, and strong nonlinearity of the coupling between fracture permeability and hydraulic aperture (Fu et al., 2017; Culp et al., 2017; Salimzadeh et al., 2017; Salimzadeh et al., 2018; Gheibi et al. 2018; Mollaali et al., 2019; Yan et al., 2020), but substantially simplify fluid flow characteristics unique to supercritical CO_2 flow in a saline reservoir. The works of Fu et al. (2017) and Yan et al. (2020) focused on modeling isothermal fluid flow in porous media and ignored the thermal responses of fractures in the storage reservoir. However, these responses have a great impact on caprock integrity (Vilarrasa et al., 2014; Salimzadeh et al., 2018). The simulations conducted by Salimzadeh et al. (2018) used a surrogate flow model—single-phase flow model— for simulating two-phase CO_2 flow, neglecting the pressure- and temperature-dependency of the PVT (pressure, volume, temperature) properties and multiphase flow of supercritical CO_2. In addition to discrete fracture models used by the above studies, smeared fracture models, such as the phase field method (Francfort and Marigo, 1998; Francfort et al., 2008), have also been adapted to address hydraulic fracturing related to CO_2 injection. Although it is straightforward to integrate the mass and energy conservations of CO_2 into the general formulation of the phase field method and to consider complex fracture processes (e.g. Culp et al., 2017; Mollaali et al., 2019), the smearing nature of this approach, nonetheless, poses stringent requirements on mesh refinement and adaptivity to accurately reconstruct the displacement discontinuities across the fracture surface (Lecampion et al., 2017). This numerical challenge limited the application of the phase field to small-scale simulations (Mollaali et al., 2019). According to the latest review on the modeling of caprock integrity (Paluszny et al. 2020), a fully coupled 3D model that can capture the complex interplay among CO_2 injection, reservoir responses, and the propagation of hydraulic fractures in a field-scale is not available yet. The scarcity of such models is likely owing to the lack of a modeling scheme that can effectively and efficiently simulate the inherent complexity of hydraulic fracturing in marginal-permeability GCS reservoirs.

The objective of this study is to develop a modeling scheme that effectively and efficiently simulates hydraulic fracturing in GCS reservoirs and to study the mechanisms of fracture containment within the caprock formations. The proposed scheme is particularly designed to simulate the interactions between coupled THM processes in a CO_2 storage system (reservoir and caprock) and the propagation of a fluid-driven fracture in the so-called “leakoff-dominated”

regime (Bunger et al., 2005; Garagash et al., 2011). As revealed by Fu et al. (2017), hydraulic fracture propagation driven by CO_2 injection into a storage reservoir is expected to be in this regime, in which the majority of the injected fluid leaks through the hydraulic fracture into and is stored in the storage reservoir. The propagation rate of the fracture is dominated by the leakoff rate into the reservoir. Mechanical responses of the fracture do not strongly affect the propagation rate, in sharp contrast to fracture behavior in the so-called storage-dominated and toughness-dominated regimes. This particular feature enables us to couple hydraulic fracturing and the associated rock deformation with reservoir flow in a simple yet sufficiently accurate way.

This paper proceeds as follows. Section 2 describes the mathematical formulations of a coupled THM model and the proposed modeling scheme that couples the THM model with a fracture mechanics module. The underlying rationale of this scheme is also discussed in this section. Section 3 validates the proposed scheme by comparing numerical results against the PKN solution in the leakoff-dominated regime. In Section 4 we build a 3D field-scale model, loosely based on the In Salah Project and reveal complex interplays between hydraulic fracturing and thermo-poroelastic effects induced by cold CO_2 injection. Section 5 discusses the effects of various reservoir conditions in the context of CGS, on the controlling mechanisms of the growth of caprock fracture. In the concluding section, we suggest possible implications of the proposed method and findings for GCS site characterization and operation.

2 Methodology

In this section, we briefly describe the governing equations of the coupled THM processes taking discrete hydraulic fractures into account. Next, we introduce the coupling scheme that links the coupled THM model to a fracture mechanics module in a simple yet accurate fashion. Note that the THM model used here is an extension of the continuum based THM model as described in Fu et al. (2020). More details related to that THM model, such as derivation of governing equations of multiphase multicomponent flow and heat transfer, numerical discretization, and fixed-stress iterative scheme, can be found in Fu et al. (2020). Moreover, the detailed descriptions of implementing the fracturing module used in this study can be found in Fu et al. (2013) and Settgast et al. (2017).

Governing equations of the THM model

As presented in Fig.1, we consider a permeable body Ω bounded by the external boundary Γ that contains Dirichlet and Neumann boundary conditions for geomechanical (traction boundary Γ_t and displacement boundary Γ_u) and flow problems (prescribed pressure/temperature boundary Γ_{PT} and flux boundary Γ_F), respectively. Specifically, for a geomechanical problem, Γ is subjected to the prescribed traction $\bar{\boldsymbol{t}}$ and displacement $\bar{\boldsymbol{u}}$ applied on Γ_t and Γ_u, respectively. For flow problem, prescribed thermodynamic conditions such as pressure $\bar{P}$, and fluxes of mass or heat ($\bar{\boldsymbol{F}}$) are applied on Γ_{PT} and Γ_F, respectively.

Domain Ω also contains an internal boundary Γ_f, where a growing fluid-driven fracture in response to the injected mass q_inj are applied. Γ_f describes the fracture whose unit direction vector $\boldsymbol{n}_\mathrm{f}$ is orthogonal to Γ_f and consists of two opposing surfaces Γ_f^+ and Γ_f^- as shown in Fig.1. The body is assumed to be permeable so that leakage $\boldsymbol{F}_\mathrm{f}$ can occur from the fracture to the surrounding body through Γ_f if a positive pressure difference from the fracture to the body is present or vice versa. Note that the process of leakoff is illustrated in the enlarged inset in Fig.1.

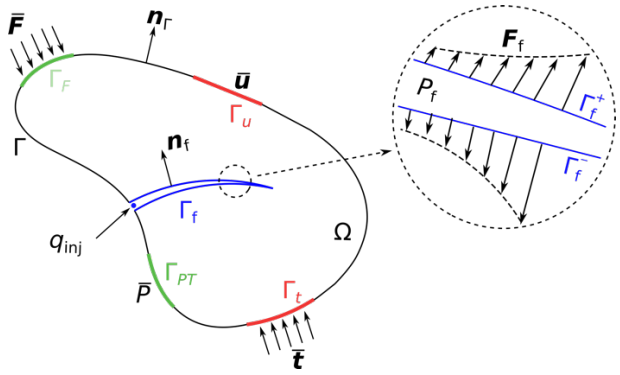

Fig. 1. Conceptual schema for modeling the evolution of a fluid-driven fracture in a permeable medium. Ω is a permeable body with an external boundary Γ that contains Dirichlet and Neumann boundary conditions for both geomechanical and flow problems. The evolving fracture in response to the injection fluid of q_inj is represented as an internal boundary Γ_f, highlighted in blue. The enlarged inset illustrates the leakoff of fluids $\boldsymbol{F}_\mathrm{f}$ in the fracture through Γ_f.

The reservoir rock and the overlaying/underlying rocks (both caprock and basement) are treated as porous media subjected to fluid/heat flow as well as poromechanical deformation. The

mathematical formulations and discretization strategy of the THM model are based on the following set of assumptions and treatments.

- For the fluid flow and heat transfer model, the movements of mobile phases through fractures and matrix are assumed to follow lubrication theory (Witherspoon et al., 1980) and Darcy's law, respectively.
- For the geomechanical model, the deformation of porous rock matrix is assumed to be quasi-static and linearly elastic. We use the small deformation assumption for the stress-strain relationship.
- Fractures and porous matrix are represented using separate but associated meshes: Fractures are represented with planar elements in the 3D space while the matrix is represented with solid elements. Mapping between the two meshes is generated as the solid mesh is split to create the fracture mesh.

Additional assumptions and treatments associated with multiphase flow and heat transport model are identical to ones adopted in Fu et al. (2020).

Geomechanical model

The governing equations for quasi-static solid deformation of a permeable body Ω can be expressed as

$$\nabla \cdot \boldsymbol{\sigma} + \rho_{\mathrm{m}}\mathbf{g} = \mathbf{0} \tag{1}$$

where $\nabla \cdot$ is the divergence operator; $\boldsymbol{\sigma}$ is the second-order total stress tensor; and $\rho_{\mathrm{m}} = \phi \sum_{J=\mathrm{A,G}} S_J \rho_J + (1-\phi)\rho_{\mathrm{s}}$ is the bulk density of matrix, in which subscript J denotes a phase of component κ (i.e., the aqueous (A) or gaseous (G) phase), S_J is the saturation of phase J, ϕ is the true porosity, and ρ_{s} is the grain density; and $\mathbf{g}$ is the gravity vector.

Based on the thermo-poroelasticity theory (Biot 1941; Coussy 2004) and the assumptions of linearly elastic and small deformation, $\boldsymbol{\sigma}$ can be related to the temperature field and displacement field:

$$\boldsymbol{\sigma} = \boldsymbol{C}_{dr} : \nabla \boldsymbol{u} - bP_{\mathrm{E}}\mathbf{1} - 3\alpha_{\mathrm{L}}K_{\mathrm{dr}}dT\mathbf{1} \tag{2}$$

where $\boldsymbol{C}_{dr}$ is a fourth-order elastic tensor, associated with the drained-isothermal elastic moduli; ∇ is the gradient operator; $\boldsymbol{u}$ is the solid displacement vector, also the primary unknown of geomechanical model; b is Biot's coefficient; $\mathbf{1}$ is a second-order identity tensor; α_{L} is the linear coefficient of thermal expansion; K_{dr} is the drained-isothermal bulk modulus; $P_{\mathrm{E}} = \sum_J S_J P_J - \int_{S_{\mathrm{A}}}^{1} P_{\mathrm{c}}(S)\mathrm{d}S$ is the equivalent pore pressure (Coussy 2004), in which P_J is the fluid pressure of phase J and P_{c} is the gas-water capillary pressure as a function of aqueous saturation; and $dT = T - T_{\mathrm{ref}}$ is the temperature difference, in which T is the current temperature and T_{ref} is a reference temperature.

In the geomechanical model, we consider the fluid pressure in the fracture, P_{f}, as a normal traction exerted on the fracture faces, Γ_{f}, while neglect the shearing traction of the fluid on solid matrix. Therefore, the traction balance across the fracture surface can be written as

$$\boldsymbol{t}_{\mathrm{f}} = -P_{\mathrm{f}}\boldsymbol{n}_{\mathrm{f}} \text{ on } \Gamma_{\mathrm{f}} \quad (3)$$

The external boundary conditions of traction and kinematic are governed by

$$\bar{\boldsymbol{t}} = \boldsymbol{\sigma}\boldsymbol{n}_t \text{ on } \Gamma_t, \quad (4)$$

$$\overline{\boldsymbol{u}} = \boldsymbol{u} \text{ on } \Gamma_u, \quad (5)$$

Where $\boldsymbol{n}_{\mathrm{f}}$ and $\boldsymbol{n}_t$ are the normal unit vectors exerted onto Γ_{f} and Γ_t, respectively; $\overline{\boldsymbol{u}}$ is the prescribed displacement on Γ_u.

Multiphase multicomponent flow and heat transfer model

The formulations of mass-and-energy conservations can be expressed in a unified integrodifferential form as:

$$\frac{d}{dt}\int_{\Omega_\alpha} M_\alpha^\kappa \, d\Omega_\alpha + \int_{\Gamma_\alpha} \boldsymbol{F}_\alpha^\kappa \cdot \boldsymbol{n} \, d\Gamma_\alpha = \int_{\Omega_\alpha} q_\alpha^\kappa \, d\Omega_\alpha, \quad \kappa \equiv \mathrm{c, w, \theta}; \quad \alpha \equiv \mathrm{m, f} \quad (6)$$

where subscript α denotes a type of flow model (i.e., matrix flow model when α = m, and fracture flow model when α = f); superscript κ denotes a component (i.e., CO_2 when κ = c, and water when κ = w) or heat (when κ = θ) in porous media, respectively.

For the matrix flow model (α = m), the formulation is identical to the one given by Fu et al. (2020). For the fracture flow model (α = f), the mass accumulation term M_{f}^{κ} integrating over an arbitrary volume of a fracture is given by:

$$M_{\mathrm{f}}^{\kappa} = \int_{\Gamma_{\mathrm{f}}} \sum_{J=\mathrm{A,G}} S_J \rho_J X_J^{\kappa} \, w^h \, d\Gamma_{\mathrm{f}} \tag{7}$$

where X_J^{κ} is the mass fraction of component κ in phase J. ρ_J is the density of phase J, respectively. The volume of a fracture Ω_{f} is assumed to be the product between its surface area Γ_{f} and hydraulic aperture w^{h}, represented by the gray volume in Fig. 2(a), which can be expressed as:

$$w^{\mathrm{h}} = (\boldsymbol{u}^{+} - \boldsymbol{u}^{-}) \cdot \boldsymbol{n}_{\mathrm{f}} \tag{8}$$

where $\boldsymbol{u}^{+} - \boldsymbol{u}^{-}$ is the discontinuity in the displacement field across Γ_{f}. Eq. (8) provides a direct coupling between the displacement field and the fracture flow.

Employing the assumption of the lubrication theory for fluid flow in fractures yields the mass fluxes term of different components, $\boldsymbol{F}_{\mathrm{f}}^{\kappa}$, expressed as

$$\boldsymbol{F}_{\mathrm{f}}^{\kappa} = -\sum_{J=\mathrm{A,G}} \rho_J X_J^{\kappa} \frac{(w^h)^2}{12\mu_J} \nabla P_J \tag{9}$$

where μ_J denotes the dynamic viscosity of fluid in phase J; ∇P_J is the fracture pressure gradient in phase J. All mass-and-heat fluxes through a fracture surface are determined via looping through its edges and summing fluxes from its neighboring surfaces. The transmissivity between fracture surfaces of different aperture is computed following the treatment given in Pruess and Tsang (1990). The mass-and-heat fluxes due to leakoff processes (as illustrated in the inset of Fig.1) can be written, using Darcy's law by assuming a Newtonian flow, as:

$$\boldsymbol{F}_{\alpha}^{\kappa} = -\sum_{J=\mathrm{A,G}} \rho_J X_J^{\kappa} \frac{k_J^{\mathrm{r}}}{\mu_J} \boldsymbol{k} (\nabla P_J - \rho_J \mathbf{g}) \tag{10}$$

where $\boldsymbol{k}$ is the intrinsic permeability tensor of matrix elements adjacent to a fracture face. Eq. (10) shows the transmissivity of the leakoff term principally depends on the hydraulic properties of the matrix elements and the corresponding leak-off area is equal to Γ_{f}.

For the component of water in the aqueous phase, the Dirichlet (in terms of fluid pressure $\bar{P}$) and Neumann boundary conditions (in terms of mass flux $\bar{\boldsymbol{F}}$) for the coupled thermo-hydro problem can be expressed as follow:

$$\bar{F} = \boldsymbol{F}_{\alpha}^{\mathrm{w}} \boldsymbol{n}_F \text{ on } \Gamma_F, \tag{11}$$

$$\bar{P} = P_A \text{ on } \Gamma_{PT}, \tag{12}$$

where $\boldsymbol{n}_F$ is the normal unit vectors exerted onto Γ_F; Γ_F and Γ_{PT} are the fixed mass flux and fluid pressure boundaries in the matrix, respectively.

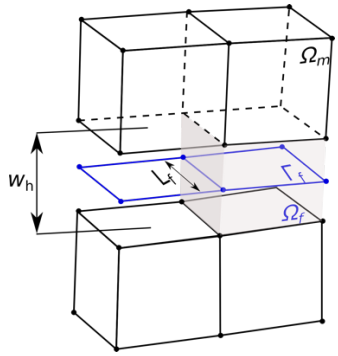

Fig. 2 Illustration of spatial discretization for coupled fracture-matrix flow model. Simulation domains of fracture are displayed in blue whereas matrix in grey.

Thermo-poromechanics

We employ the fixed-stress iterative scheme to solve thermo-poromechanics in rock matrix (Kim et al., 2011). In this scheme, the coupled THM problem splits into two subproblems, i.e. a fluid-heat flow problem and a geomecahnical problem. During each iteration, the subproblems are solved in an iterative sequence until the convergence of both problems. Particularly, in solving the fluid-heat flow problem, the current true porosity is estimated from its previous state with the following equation and assuming the rate of total volumetric stress remain unchanged throughout the current time step.

$$d\phi = \frac{b-\phi}{K_{\mathrm{dr}}}(dP_{\mathrm{E}} + d\boldsymbol{\sigma}_{\mathrm{v}}) + 3\alpha_{\mathrm{L}} b dT \tag{13}$$

where $\boldsymbol{\sigma}_{\mathrm{v}}$ is volumetric total stress.

The numerical treatment of implementing the fixed-stress iterative scheme follows the same procedure described in Fu et al. (2020).

Fracture mechanics module

We adopt the fracture mechanics module of GEOS, a high-performance computing simulation code (Fu et al. 2013; Settgast et al. 2016; Ju et al., 2020), to simulate fracture propagation. This module uses linear elastic fracture mechanics and a modified virtual crack closure technique (MVCCT) to calculate energy release rate G at fracture tip (Huang et al., 2019). Fracture extends from tip to intact rocks when G exceeds the critical value G_c, which can be related to the critical stress intensity factor K_{IC}, also known as fracture toughness, through

$$G_c = K_{Ic}^2\left(\frac{1-\nu^2}{E}\right) \tag{14}$$

When fracturing occurs, new fracture faces are created by splitting the nodes between the two solid elements adjacent to the tip faces. As mentioned in the previous section, the fluid pressure along fracture is applied onto the solid elements that are connected with those faces as normal traction. Properly implementing this traction boundary condition is essential for satisfying the momentum balance of solid elements in the updated mesh topology. Moreover, the fluid-heat flows in newly created faces are automatically integrated into the matrix-fracture flow system, ensuring the mass-and-energy balance across the entire domain.

The coupling scheme between THM model and fracture mechanics module

The three main components of our model, (1) the multiphase multi-component solver for porous medium and fracture flow, (2) the hydraulic fracturing module, and (3) the poromechanics solver, are all known to face their own numerical challenges (Kim and Moridis 2013; Settgast et al., 2016; White et al., 2016). These modules are challenging even under more amiable conditions, namely without the complication of fracturing for the first component and when the latter two only deal with single-phase flow. In prior works, we have developed relatively robust individual modules on a common platform, GEOS, for these three components (Settgast et al., 2016; Fu et al., 2020). Still, coupling these three components together is evidently an extremely challenging task.

It is widely acknowledged that an implicit coupling strategy theoretically provides unconditionally convergent numerical solutions and enables large timesteps for the preceding

coupled problem (Kim et al., 2012; Girault et al., 2016). However, the actual implementation to implicitly couple the three aforementioned modules faces practically insurmountable numerical difficulties, exacerbated by challenges associated with the parallel computing environment. We therefore develop a sequential coupling scheme to take full advantage of existing modules in GEOS. Meanwhile, as sequential coupling often suffers from difficult convergence, we utilize some self-stabilizing features of leakoff-dominated fracturing to simplify the coupling scheme.

In this scheme, we use a compositional reservoir simulator for solving fluid-heat flow problem and a standard Galerkin finite element method for geomechanics. As mentioned in section 2.1.4, fracture mechanics module evaluates fracturing criterion as well as updates solid mesh and flow network once new fracture surfaces are generated. The sequential communication between the THM model and fracture mechanics module is achieved by sharing key information, such as fluid pressure in fractures and displacement fields, at every timestep (see Fig. 3). This procedure can be performed without compromising the modularity of the code because only minor modifications are required for existing individual modules.

The relationships among the physical processes involved in the problem are summarized in Table 1. Several interactions have been implicitly handled in existing modules. For instance, the fracture flow and matrix flow are solved together by unifying the fracture flow network and the matrix flow mesh in a combined flow topology as shown in Figure 2. In other words, in the cell-centered finite volume framework, both the flow "faces" for fracture flow and the solid "elements" for matrix flow are considered "cells" interconnected together. Also, the solid deformation and matrix flow are already coupled using the "fixed-stress" scheme in the poromechanics solver. The remaining relationships are enforced sequentially as shown in Figure 3.

An inconsistency and thereby an error are introduced in the coupled solution flow. In the n^{th} iteration of each time step, the aperture is computed in Steps 3 and 4 based on the geomechanical module's results. In iteration n+1's Step 1, the initial "guess" of the fracture cells' states is based

on the solved pressure from Step 1 and the aperture from Steps 3 – 4 of iteration *n*. Therefore, the aperture update in iteration *n* would introduce a small extra (positive or negative) fluid mass to the system. We found this treatment is greatly beneficial for the convergence of the solution for the following reason. An open fracture's aperture is extremely sensitive to fluid pressure. If we use the fluid mass in each fracture cell from iteration *n*'s Step 1 while using the updated aperture, the initial "guess" of the flow system's state in iteration *n*+1 would be highly volatile and usually far from the "true" solution, resulting in severe difficulties in convergence. We hypothesize that this inconsistency is inconsequential for the overall accuracy of the solved system because only a very small fraction of the injection fluid is stored in the fracture, a salient feature of the leakoff-dominated regime. In the verification solution in Section 3 and simulation results in Section 4, we compare the total masses of CO_2 in the numerical models with the total injected quantities to quantify the induced error. Note that rock porosity is not very sensitive to pressure change, so this treatment is unnecessary for the rock matrix cells.

Table 1. Coupling relationships between individual modules. The "step" in each cell refers to an "operation" in the flow diagram in Figure 3 where the interaction is embodied.

Modules providing information	Modules receiving information			
	Fracture Flow	Matrix flow	Solid deformation	Fracture mechanics
Fracture Flow	Self	Pressure boundary condition along fracture faces; solved together.	Traction boundary condition along fracture faces. Step 2.	Indirect influence, through solid deformation
Matrix flow	Fluid leakoff; solved together	Self	Solved together in poromechanics	Indirect influence, through solid deformation
Solid deformation	Hydraulic aperture and fluid storage. Step 4.	Solved together in poromechanics	Self	Compute energy release rate. Step 0.
Fracture mechanics	New fracture flow elements. Step 0.	Indirect influence, through fracture flow	Updated mesh. Step 0.	Self

We found the sequential coupling scheme to have satisfactory numerical performance: Most time steps converge within five iterations; The scheme is stable as long as the time step is significantly smaller than the time that it takes the fracture to propagate the distance of one-element length. This is again largely owing to the self-stabilizing features of fracture propagation in the leakoff-dominated regime: As the permeability of the reservoir is largely

constant, the leakoff rate is mostly determined by the difference between fluid pressure in the fracture and the far-field fluid pressure in the reservoir. In a propagating fracture, the fluid pressure is always marginally higher than the "fracture propagation pressure", which, in the scenarios concerned by this study, is approximately the "fracture opening pressure" near the fracture front. The fracture opening pressure is in turn determined by the total stress in the system, which evolves very slowly. Therefore, a convergent numerical solution can be obtained as long as the effects of the extending fracture surface area on the flow into the rock matrix are captured.

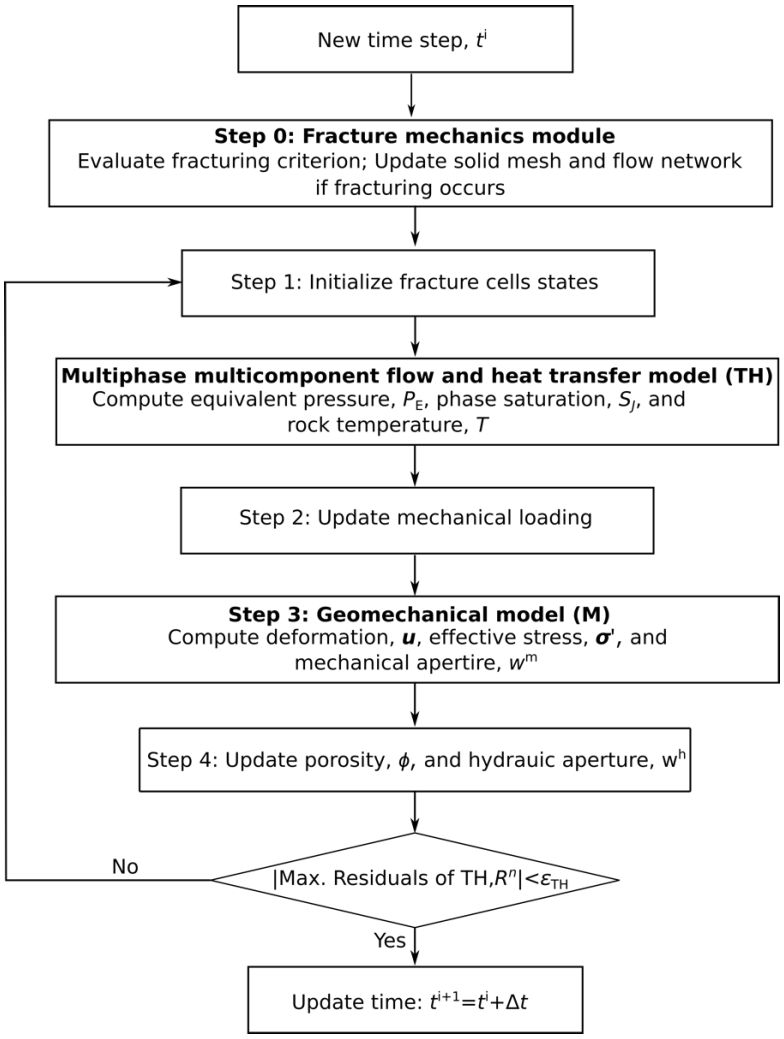

Fig. 3. Flowchart of the coupling scheme between coupled THM coupled model and fracture mechanics module. The coupling convergence criterion of coupled THM model is that the maximum residuals of TH model is smaller than ε, a pre-set small value, say 1e-5, after updating perturbed hydraulic variables.

Verification

In this section, we compare the new model's results with the PKN solution in the leakoff-dominated regime to verify the numerical implementation of the model and, particularly, to validate the coupling scheme presented in Section 2.2.2. Note that the validation of relevant individual submodules in GEOS has been reported in previous works, in which numerical results are compared with the analytical solutions of poromechanics (Terzaghi's and Mandel's problems (Fu et al., 2019; Fu et al., 2020)), and of fracturing propagation in different regimes (Fu et al., 2013; Settgast et al., 2017).

The PKN solution in the leakoff-dominated regime

We use a standard fracture geometry, the PKN model as illustrated in Fig. 4(a), to test the proposed coupling scheme (Perkins and Kern 1961; Nordgren 1972). The origin of the coordinate system is set at the injection point; the *x*-direction coincides with the fracture propagation direction, so the y-axis is along the direction of the minimum principal *in situ* stress S_{hmin}. Recall that hydraulic fracturing in a storage reservoir with moderate permeability is in the leakoff-dominated regime. We therefore compare the numerical solutions against the PKN model in the so-called leakoff-dominated regime (Nordgren 1972). This solution describes the growth of a fixed-height vertical fracture when the volume of fluid loss into reservoirs is much larger than the volume stored in the fracture.

According to the analytical solution (Nordgren 1972), the half fracture length L_{f} and aperture w_0^{h} at wellbore are

$$L_{\text{f}} = \frac{qt^{1/2}}{2\pi C_{\text{L}} h_{\text{f}}} \tag{15}$$

$$w_0^{\text{h}} = 4\left[\frac{\mu q^2}{\pi^3 E' C_{\text{L}} \text{h}_{\text{f}}}\right]^{\frac{1}{4}} t^{1/8} \tag{16}$$

where q is the total injection rate; h_{f} is the fracture height; $E' = E/(1\text{-}\nu^2)$ is the plane-strain modulus for the formation; and C_{L} is the Carter's leakoff coefficient. As revealed in Howard and Fast (1957), C_{L} can be expressed as:

$$C_{\mathrm{L}} = \Delta P\left(\frac{k_{\mathrm{r}}\phi c_t}{\pi\mu}\right)^{1/2} \tag{17}$$

where ΔP is the difference between the fracture pressure and the remote reservoir pressure that is assumed to be constant; k_{r} is the intrinsic permeability of reservoir; and c_t=c_{f}+c_{p} is the total compressibility, where c_{f} is fluid compressibility and c_{p} is pore compressibility, both of which are constants in equation (17). However, in a high-fidelity numerical model, c_{f} and c_{p} respectively depend on the nonlinear PVT properties of fluids and the solid deformation in the coupled THM models. Therefore, when applying the analytical solution, we set c_t at the value computed from the numerical models for simplicity. Also note that equation (17) is based on the assumption of 1D diffusion, which is not necessarily valid in a real reservoir or in a high-fidelity numerical model.

Some additional special adaptations of the numerical model are needed to be consistent with assumptions of the analytical solution. The analytically solution intrinsically assumes zero toughness for the reservoir rock. Accordingly, we set the toughness of reservoir rock to 100 Pa $\mathrm{m}^{1/2}$, a small finite value that prevents small numerical noise from triggering fracturing. The analytical solution calculates leakoff using the Carter's leakoff coefficient, which is based on 1D diffusion. However, the fluid flow in the THM coupled model is 3D in nature. In order to match the 1D diffusion assumption, we use a strongly anisotropic permeability (k_{ry}=10 mD, k_{rx}=k_{rz}=0 mD). We also run an additional simulation by removing the 1D diffusion restriction for comparison. Moreover, the Biot coefficient is set to zero in the numerical model, since the PKN model does not incorporate the poromechanical effects in the reservoir. Note that none of the above adaptations is used in the 3D simulations in section 4 and beyond.

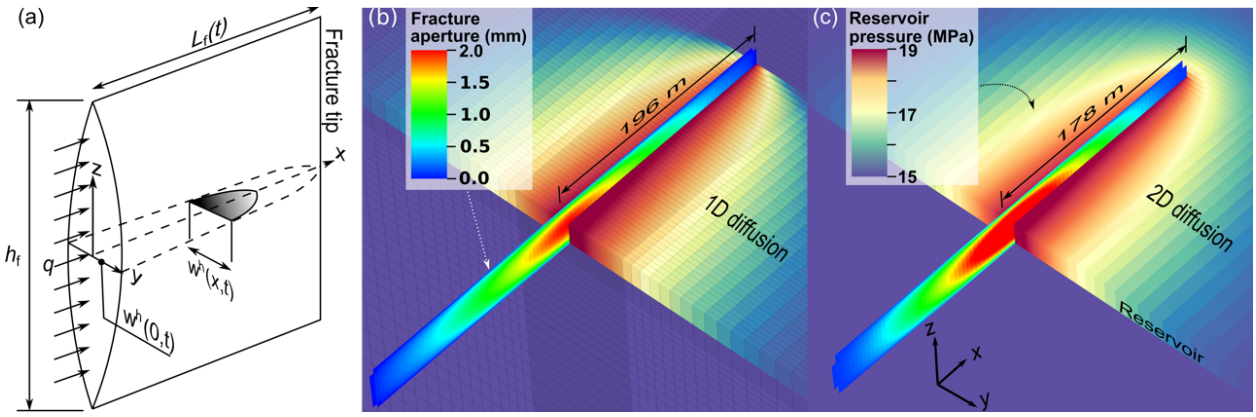

Fig. 4. Geometrical characteristics (a) and simulation results for a PKN fracture with q=0.04 m^3/s in the case of (b) 1D diffusion and (c) 2D diffusion at t=4×10^{5}s. In (a) where only one wing of the fracture is shown due to symmetry, h_f, q, w^h, and L_f indicate fracture height, injection rate, fracture width(aperture), and fracture length, respectively. In (b) and (c), a full length/height of the fracture and a quarter of the reservoir pressure field are presented. Note that fracture color scale indicates fracture aperture, whereas the color scale for the matrix indicates reservoir pressure.

Numerical realization of the PKN model

The numerical simulation only models one quarter of the problem owing to the symmetrical condition of PKN model, as shown in Fig. 4(a). To minimize boundary effects, the dimensions of the quarter model are 1000m, 2000m, and 1000m in x-, y-, and z-directions, respectively, where meshing in each dimension contains a refined portion (200m, 100m, and 40m in x-, y-, and z-directions, respectively) and coarse portion. The refined region uses constant mesh resolutions in three directions, i.e. 4m, 1m, and 2m, respectively, whereas the coarse region uses a progressively coarser mesh resolution toward the far-field. The model is discretized into 1,004,731 hexagonal elements. We simulate fracture propagation and reservoir response for three different injection rates as listed in Table 1. The fourth simulation removes the 1D diffusion restriction for the baseline injection rate and results are denoted by "2D diffusion" in Fig. 4 and 5. Parameters adopted in the verification are listed in Table 1.

Table 1. Parameters employed in the numerical model for the simulation of the PKN model.

Property	Value
Fracture height, H_f	40 m
Injection rate, q	0.02, 0.04[a], and 0.06 m^3/s
Dynamic viscosity, fluid, μ	1×10^{-3} Pa s
Porosity, ϕ	0.2
Pore compressibility, c_t	1.04×10^{-8} Pa^{-1}
Poisson's ratio, v	0.25
Biot's coefficient, b	0.0
Carter's leakoff coefficient, C_L	0.493 mm/$\sqrt{s}$
Young's modulus, E	10 GPa
Critical stress intensity factor (toughness), reservoir	100.0 Pa•m$^{0.5}$

[a]baseline case simulation

Verification results

Fig. 5 shows a comparison of results from the numerical simulation and the PKN solutions. In general, the temporal evolution of fracture length for the three injection rates are in good agreement with the corresponding analytical solutions. The numerically simulated apertures tend to deviate from the analytical solutions early in the injection but gradually converge to the solutions as injection progresses.

The disparity between the numerical solution and the PKN solution at the early times is likely caused by the geometric assumptions of the PKN model, i.e. the fracture length being much larger than the fixed fracture height (a rectangular fracture shape). In the early stage of injection, the fracture length simulated by the numerical model, however, is smaller than or similar to the preset fracture height, forming a penny shape and therefore a direct comparison between solutions with different fracture shape assumptions is not appropriate. Note that for all the three injection rates, the numerically predicted apertures become very similar to the analytical solutions when the half fracture length in each case reaches around 200 m, 2.5 times the fracture height. Fig. 5(b) also shows that numerical results of wellbore aperture exhibit a moderate oscillatory behavior. This behavior is expected because the spatial discretization scheme dictates that the fracture has to propagate by the length of an element, yielding numerical overshoot/undershoot.

As shown in Fig. 5(c), the percentage of fluid in the fracture compared with the total injection volume, termed "*fracture volume ratio*" in this study, is quite low, mostly less than 1%. This confirms that these four simulated hydraulic fractures are indeed in the leakoff-dominated regime. Note that the "fracture volume ratio" is mathematically identical to the "fluid efficiency" used in unconventional reservoir stimulation. However, we avoid using this established term because in carbon storage, retaining more fluid in the fracture, i.e. achieving a "high fluid efficiency", is not an objective.

Fig. 5(d) shows the temporal evolution of "*mass loss ratio*", defined as the percentage of mass loss induced by the coupling scheme compared with total injection mass in this study. Note that a negative mass loss ratio means extra masses are introduced in the system. At the early stage of

injection, when the fracture volume ratios are high, some extra masses, albeit very small, are either introduced or lost in the system. However, those inconsistencies rapidly diminish, and the absolute mass losses converge to near zero as the leakoff becomes predominant. The convergence of mass loss ratio for each case validates our hypothesis that the mass loss induced during the coupling is indeed trivial and proves the accuracy of our coupling scheme for simulating the leakoff-dominated fracturing.

The comparison between Fig. 4(b) and (c) shows the fracture length grows faster in the case of 1D diffusion than that of 2D diffusion where the front of reservoir pressure plume goes further than the crack tip. Likewise, Fig.5 (a) and (c) shows that the case of 2D diffusion yields a slightly higher leakoff compared with the baseline verification (1D diffusion), which includes lower fracture growth rate and smaller wellbore aperture. Those behaviors are mainly owing to the overestimation of the actual C_L when 2D diffusion is invoked (Carrier and Grant, 2010; Fu et al., 2017).

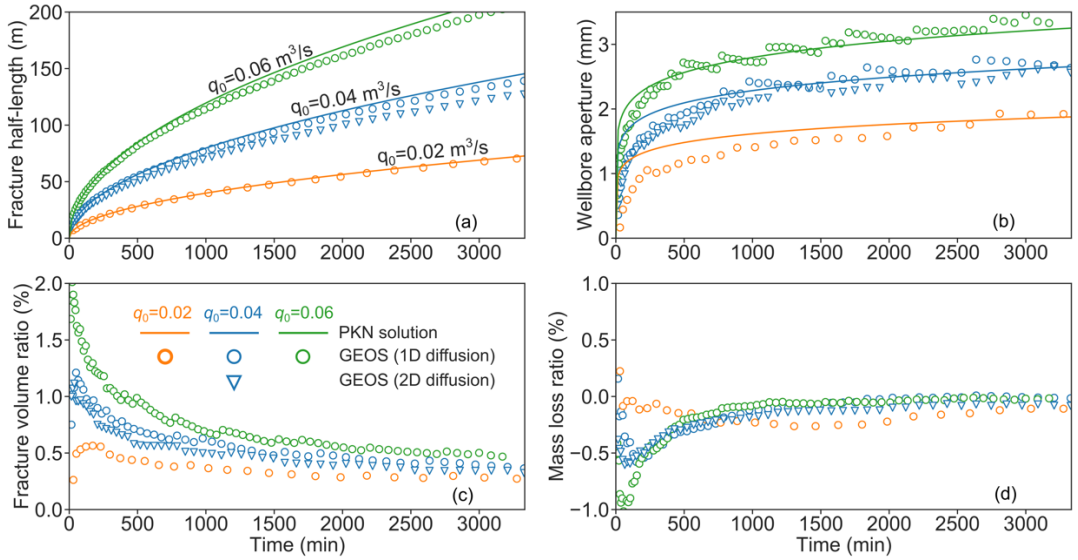

Fig. 5. Simulation results for a PKN fracture in the leakoff-dominated regime. (a), (b), (c) and (d) plot the temporal variations of fracture half-length, wellbore aperture, fracture volume ratio, and mass loss ratio respectively. Analytical solutions for leakoff-dominated fractures are plotted in (a) and (b) for comparison. The fracture volume ratio in (c) denotes the percentage of the total injected fluid stored in the fracture. The mass loss ratio in (d) denotes the percentage of the mass loss induced by the coupling scheme compared with the total injection mass.

Application in simulating fracturing into caprock

To demonstrate the simulation capacity of the proposed scheme and apply it to GCS, we build and analyze a field-scale 3D numerical model (hereafter referred to as the baseline case) in GEOS in this section. The baseline model is loosely based on the geological settings of the In Salah storage site (Rutqvist et al., 2010; Ringrose et al., 2013; White et al., 2014), as shown in Fig. 6 (a), while the analyses generally apply to a GCS reservoir with marginal permeability.

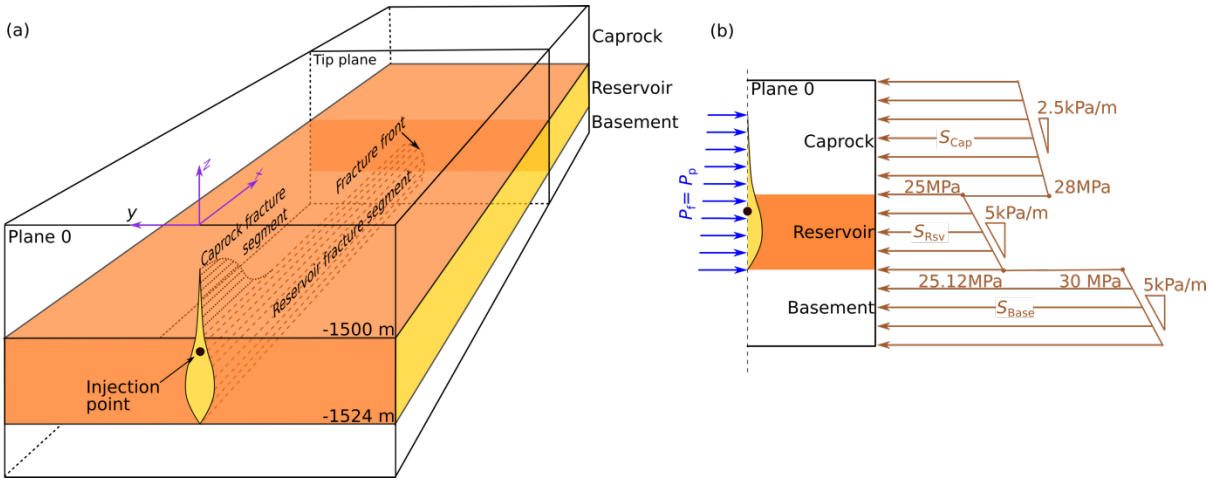

Fig. 6. (a) 3D schematic (not to scale) of the configuration, geometry and dimensions of baseline model showing one wing of a hydraulic fracture penetrating into the caprock, with cold supercritical CO_2 entering the computational domain from the injection point, marked as a black dot on the plane 0 (x=0). Tip plane tracks the movement of fracture front. Sub-figure (b) shows internal and external traction boundary conditions, i.e. fracture pressure and horizontal *in-situ* stress, applied to the 3D model on plane 0. Note that only one wing of the fracture in panel (a) is shown due to symmetry.

Model setup

Fig. 6(a) schematically depicts the 3D geometry of the baseline model. The CO_2 storage reservoir of marginal permeability is sandwiched between the caprock and the basement, both of which are much less permeable. The reservoir is 24 m thick with its interface with caprock located at 1500 m depth (z = -1500 m). We established a 3D coordinate system, in which the x-axis is parallel to the direction of the maximum *in situ* horizontal stress (S_{Hmax}), the y-axis is parallel to the direction of minimum *in situ* horizontal stress (S_{hmin}), the z-axis points upward, and the origin at ground surface resides above the injection point. The injection point is annotated as a black dot in Fig.6 (a) to highlight its position. The initial pore pressure follows the

hydrostatic distribution and the initial reservoir temperature is set as 65 °C. The minimum principal *in situ* stress (S_{hmin}) follows a segmented-linear distribution along the z direction, as shown in the right portion of Fig. 6(b). S_{hmin} distributions of caprock, reservoir, and basement layers are denotated as S_{Cap}, S_{Rsv}, and S_{Base}, respectively. We assume that there is a fracturing barrier between the reservoir and basement that prevents downward fracturing as we mainly focus on conditions and mechanisms for fracturing in the reservoir and caprock. As illustrated in Fig. 6(a), the fracture propagation is assumed to only take place within the x-z plane, perpendicular to the direction of S_{hmin}. Note that the symmetry of the system with respect to the y-z plane at the injection point allows the use of a half model.

Fully-saturated supercritical CO_2 at an injection temperature of 45 °C, is injected into the reservoir at a constant rate of 15.0 kg/s (one wing of fracture), approximately a million metric ton per year. We assume that the injection well is cased, and fractures are initiated from perforations, which renders the well only to communicate with the system at its interaction with the fracture. Thus, the injection well can be simplified as a point source in our 3D computational domain. The so-called "roller" boundary condition is applied to all "far-field" boundaries when initializing geomechanical model. For the fluid flow model, prescribed mass/heat rate conditions for the injection well are applied at x= 0, y=0 and z=-1502 m. We apply the original reservoir pressure and a constant ambient temperature (65 °C) at the lateral boundaries as the far-field Dirichlet boundary conditions. No-flow conditions are naturally applied to elements on the top and bottom planes.

The computational domain of the baseline case has a core region whose dimensions in x-, y-, and z-directions are 800m, 200m, and 240m, respectively. The core region has a relatively fine mesh resolution of 8.0, 4.0, and 8.0 m in those directions. Surrounding the core region is a coarsely resolved region that extends to 5800 m, ±9000m, and ±400m in the respect three directions, which mitigates boundary effects while maintaining computational efficiency. The baseline model involving a kilometer-scale reservoir and 3 years of injection time, is discretized into 1,344,000 elements and the simulation is conducted across 252 CPU cores (16

Intel® Xeon® E5-2670 CPUs), which runs for 18 hours on a high-performance computer (4536 core-hours in total).

Table 3 summarizes the computational parameters and constitutive models for the baseline model. As for the mobility-related constitutive models in multiphase flow model, we use a Corey-type relative permeability functions (Brooks and Corey, 1964) and a van Genuchten capillary function (Van Genuchten, 1980), respectively written as Eq. (18) and (19).

$$k_{\mathrm{A}}^{\mathrm{r}} = S_{\mathrm{n}}^4,\ k_{\mathrm{G}}^{\mathrm{r}} = (1 - S_{\mathrm{n}})^2(1 - S_{\mathrm{n}}^2) \qquad (18)$$

$$P_{\mathrm{C}} = -P_0[(S^*)^{-1/\lambda} - 1]^{-1/\lambda},\ S^* = (S_{\mathrm{A}} - S_{\mathrm{irA}})/(1.0 - S_{\mathrm{irA}}) \qquad (19)$$

where $k_{\mathrm{A}}^{\mathrm{r}}$ and $k_{\mathrm{G}}^{\mathrm{r}}$ are relative permeabilities in aqueous and gaseous phases; $S_{\mathrm{n}} = (S_{\mathrm{A}} - S_{\mathrm{irA}})/(1.0 - S_{\mathrm{irA}} - S_{\mathrm{irG}})$ is the normalized aqueous saturation; S_{irA} and S_{irG} are the irreducible aqueous saturations and the residual gas saturations, respectively. λ and P_0 are the exponent that characterizes the capillary pressure curve and the capillary modulus, respectively. Then, we set $S_{\mathrm{irA}} = 0.12$ and $S_{\mathrm{irG}} = 0.01$ for relative permeability, and $S_{\mathrm{irA}} = 0.11$, P_0= 12500 Pa, and λ = 0.254 for capillarity, where the capillary pressure model employs a slightly smaller S_{irA} than the model of relative permeability in order to prevent unphysical behavior (Moridis and Freeman, 2014).

Table 2. Parameters employed in the baseline simulation

Property	Baseline value
Reservoir thickness, H_{r}	24 m
Minimum principal *in situ* stress in reservoir, total stress, mid-depth, $S_{\mathrm{hmin}}^{\mathrm{r}}$	25 MPa
Minimum principal *in situ* stress in caprock, total stress, mid-depth, $S_{\mathrm{hmin}}^{\mathrm{c}}$	30 MPa
Initial pore pressure, mid-depth of reservoir, P_{int} (hydrostatic condition applies)	15 MPa
Biot's coefficient, reservoir rock, b_{r}	0.5
Biot's coefficient, caprock, b_{c}	0.25
Intrinsic permeability, reservoir, k_{r}	15 mD
Intrinsic permeability, other layers, k_{c}	0.1 μD
Porosity, reservoir, ϕ_{r}	0.15

Porosity, all other layers, ϕ_c	0.05
Young's modulus, all layers, E	10 GPa
Poisson's ratio, all layers (Armitage et al., 2010), v	0.25
Initial temperature, all layers, T_{Int}	65 °C
Coefficient of thermal expansion, linear, α_L	10^{-5} /°C
Injection temperature, T_{Inj}	40 °C
Thermal conductivity, all layers, λ	3.0 W/(m·K)
Heat capacity, all layers, C_s	1000 J/(kg·K)
Critical stress intensity factor (toughness), all layers (Senseny and Pfeifle, 1984)	1.0 MPa·$m^{0.5}$
Relative permeability model[a] (Brooks and Corey, 1964)	$k_A^r = S_n^4$ $k_G^r = (1 - S_n)^2(1 - S_n^2)$ $S_n = (S_A - S_{irA})/(1.0 - S_{irA} - S_{irG})$ $S_{irA} = 0.12$, $S_{irG} = 0.01$
Capillary pressure model[b] (Van Genuchten, 1980)	$P_C = -P_0[(S^*)^{-1/\lambda} - 1]^{-1/\lambda}$ $S^* = (S_A - S_{irA})/(1.0 - S_{irA})$ $S_{irA} = 0.11$, $P_0 = 12500$ Pa, $\lambda = 0.254$

a k_A^r and k_G^r are relative permeabilities in aqueous and gaseous phases; S_n is the normalized aqueous saturation; S_{irA} and S_{irG} are the irreducible aqueous saturation and the residual gas saturation, respectively

b P_0 is the capillary modulus

Results of baseline model

As presented in Fig. 7 and Fig. 8, results of the baseline model clearly show how a leakoff-dominated fracture is driven by injection and provides an evolving interface between injection and reservoir storage. By the end of three years of injection, the fracture has propagated 620 m into the reservoir, providing a growing interface plane for feeding injected CO_2 into the reservoir. The CO_2 plume advances approximately 625 m in the y-direction each side (Fig. 8(p)), spanning an area of reservoir as large as about 1.24×1.25 square kilometers. Note that the rate of injection employed in the baseline case cannot possibly be achieved if the downhole injection pressure is strictly limited to below the estimated fracturing pressure of the caprock, approximately 25 MPa. Meanwhile, the maximum fracture height only reaches 88 m, thereby being vertically contained in the lower portion of the caprock (Fig. 7(b) and Fig. 8(m)). Note that the containment mechanism will be elucidated in the subsequent analysis.

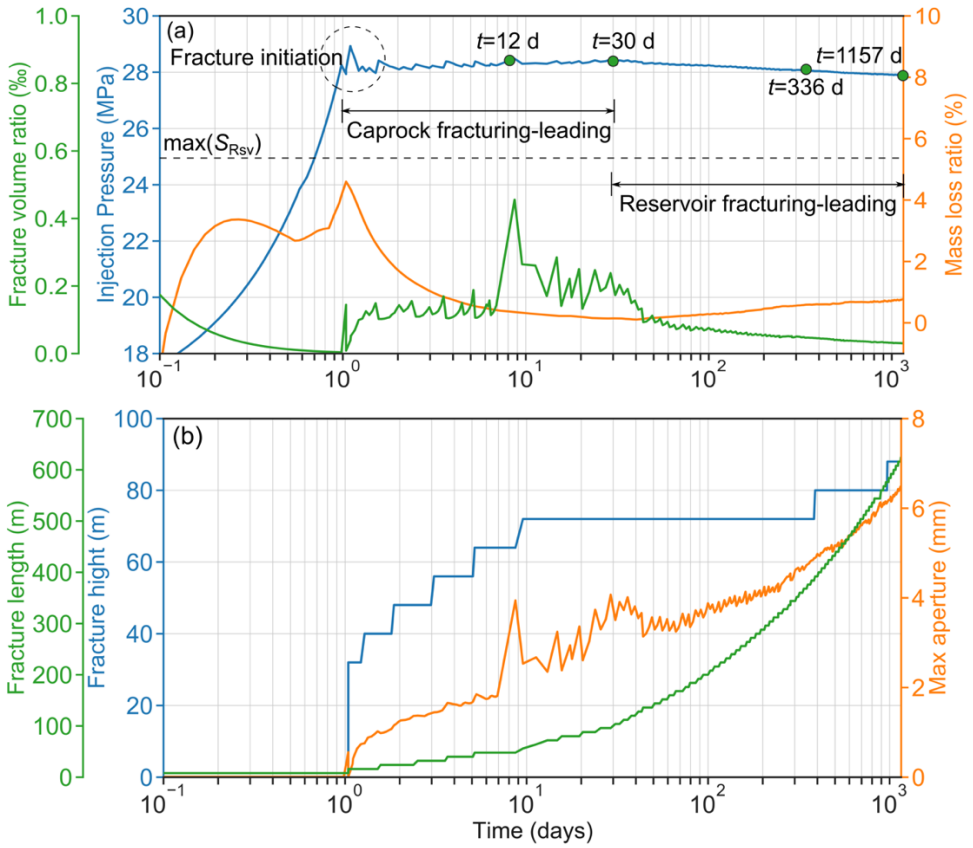

Fig. 7. Overall responses of the system in the baseline case. (a) Fracture volume ratio, injection pressure, and mass loss ratio versus time; (b) Fracture length, fracture height, and max aperture versus time. The curve colors in (a) and (b) correspond to their *y* axes. Fracture volume ratio is the percentage of injected fluid retained in the fracture. Injection pressure is measured at the injection point at the entrance to the fracture. Mass loss ratio is the percentage of injected CO_2 mass that is "lost" due to the error introduced by the sequential iteration scheme as explained in section 3.3. Note that the highest stress level of S_{Rsv}, max(S_{Rsv}), which is the in situ stress magnitude at the bottom of the reservoir, is indicated by a black dash line in (a).

Another interesting observation is the evolution of injection pressure (the blue line in Fig. 7(a)) at the entrance to the fracture over time, which can be divided into three stages: (1) the initially rapid pressure buildup before apparent fracture growth (about 1 day), (2) the pressure plateau as fracture propagates (from 1 day to 30 days), and (3) the subsequent slow pressure decline (after 30 days). In the first stage, accommodating the injection rate requires sustaining an open fracture in the reservoir, which in turn requires a continuously increasing injection pressure, much higher than original S_{Rsv}, owing to the effect of back-stresses caused by pressure diffusion into the reservoir (Detourney and Cheng, 1997; Kovalyshen, 2010). Fu et al. (2020) had modeled how

this effect causes rapid increase of injection pressure and eventually causes fracturing of the caprock.

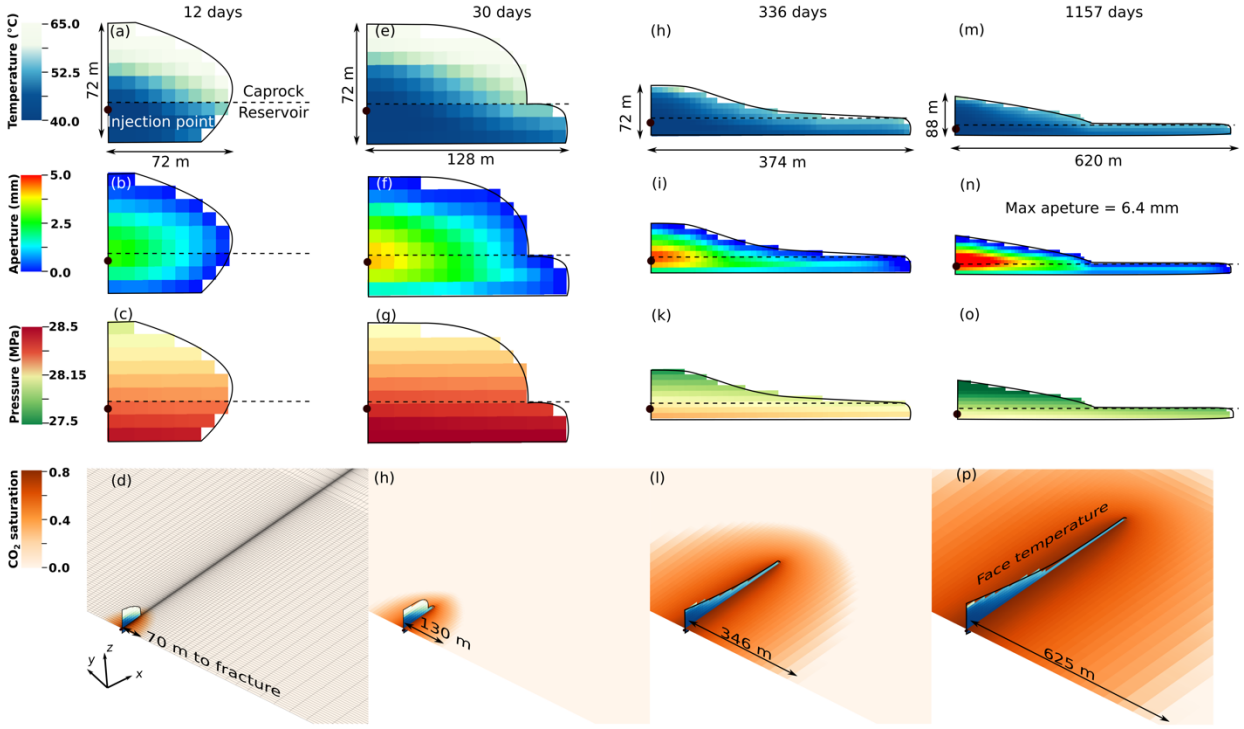

Fig. 8. Four selected states of the hydraulic fracture and the reservoir rock. The first three rows present snapshots of temperature (first row), aperture (second row), and pressure (third row) on the evolving hydraulic fracture. The last row shows the spatial-and-temporal evolution of CO_2 (critical state gas phase) in the reservoir (z=-1510 m). The interface between the reservoir and the caprock is denoted by a dark dashed line and the injection point is annotated as a black dot. Note that scales vary among the columns of the first three rows for clearer visualization, whereas the four sub-figures in the fourth row use the same scale.

Here we mainly focus on the evolution of fracture propagation after caprock fracturing takes place, which spans the second and third stages as designated in this section. Figure 8 shows four representative states of the fluid-driven fracture and CO_2 saturation (supercritical state gas phase) in the reservoir rock, at 12 days (in second stage), 30 days (transition from second to third stage), 336 days and 1157 days (both in third stage). In the second stage when the pressure is largely constant, fracturing in caprock seems to lead fracturing in the storage reservoir. The constant injection pressure in this stage reflects the fracturing pressure of the caprock, which is mainly influenced by S_{Cap}. Note that the injection pressure is only slightly higher than S_{Cap} near the reservoir-caprock interface. In the third stage, reservoir fracturing leads the fracture length

growth and the injection pressure slowly declines as explained in Section 4.2.2. This pattern change suggests an evolution of fundamental physical mechanisms that dominate fracture growth as elucidated in the subsequent sections.

Second stage: caprock fracturing-leading

Fig. 9 presents spatial distributions of the fluid pressure, temperature, effective stress, and total stress in two vertical cross-sections (near the injection and near the fracture tip, respectively) and two horizontal cross-sections (in the reservoir rock 10 m below the bottom of the caprock, and in the caprock 30 m above the top of the reservoir rock) after 12 days of injection. Pore pressure propagates in the reservoir much farther than in the caprock, due to the much higher permeability of the reservoir (150,000 times higher than that of the caprock). Significant temperature decreases only take place within a short distance from the fracture in the reservoir (Fig. 9 (e) and (f)), while temperature change in caprock is hardly perceivable (Fig. 9 (g)). Although thermo-mechanical effect tends to reduce the total stress in the cooled region in the reservoir, the effect of poroelasticity on increasing the total stress in this case is much stronger. As a result, the total stress near the fracture in the reservoir even becomes higher than in the caprock, although initial S_{hmin} in the reservoir was on average 3 MPa lower than that of the caprock. This reversed stress contrast tends to hamper fracture propagation in the reservoir, which directly entails an easier propagation in the caprock.

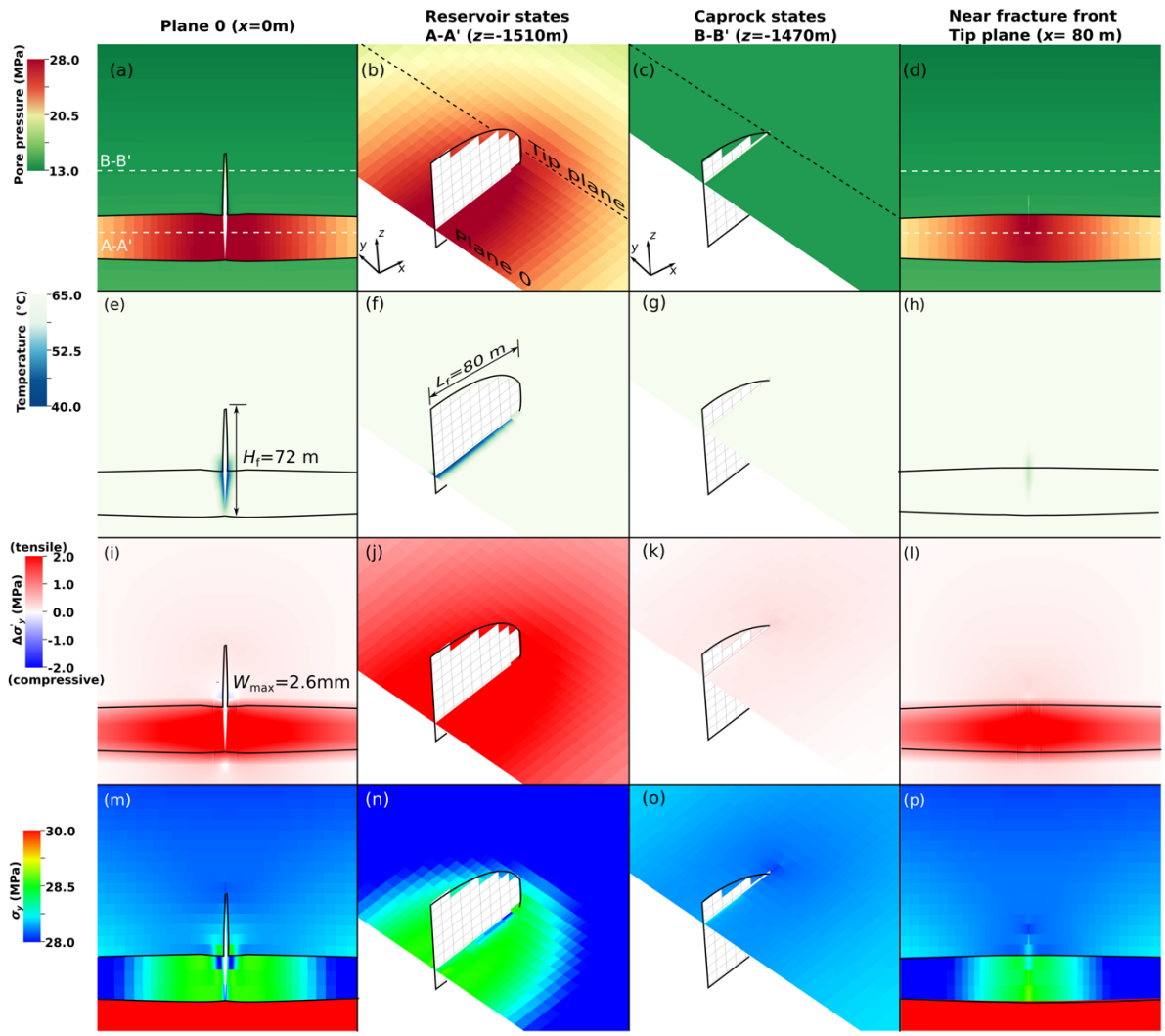

Fig. 9. States of the reservoir rock and the caprock after 12 days of injection. The four rows of panels show spatial distributions of pore pressure (first row), temperature (second row), effective stress increment (third row), and horizontal total stress (fourth row). The first and fourth columns respectively show the distributions of variables on two vertical planes cutting the injection point and the fracture tip, respectively. The second and third columns show the distributions of the variables on two horizontal planes A-A′ (reservoir) and B-B′ (caprock) respectively. The deformation of first and fourth columns is magnified by 500 times.

Third stage: reservoir fracture-leading stage

The system response in this stage is depicted using spatial distributions of the same variables as the ones used in the preceding section in a much later state, 1157 days into the injection (Fig. 10). In general, the most marked difference from the second stage is that the fracture has horizontally grown much longer, which mostly takes place in the reservoir rock, and that the

cooling front in the reservoir has advanced much further (i.e. thermal penetration depth is comparable to fracture height).

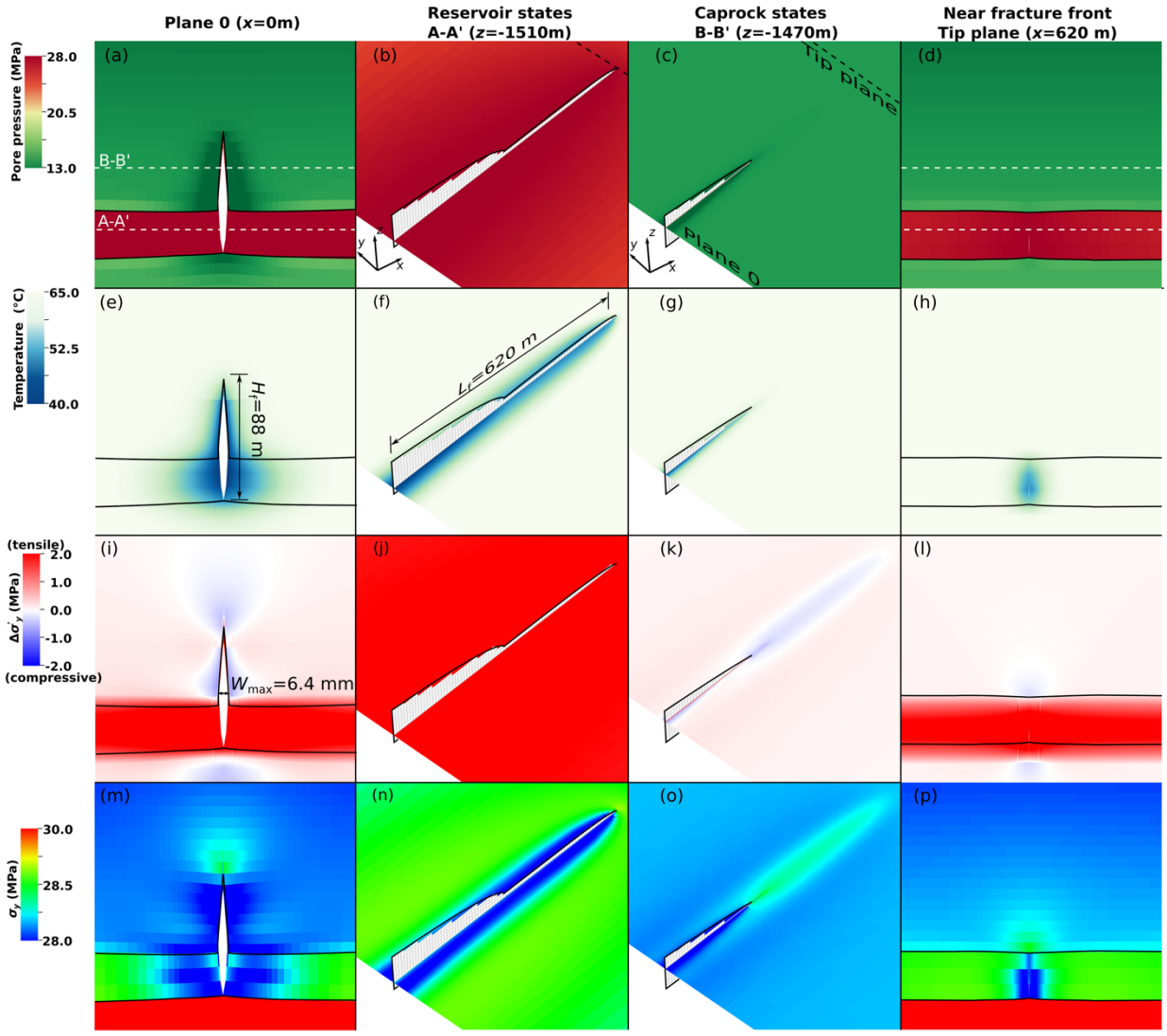

Fig. 10. States of the reservoir rock and the caprock after 1157 days of injection. The four rows of panels show spatial distributions of four variables, namely pore pressure ((a) through (c)), temperature ((d) through (f)), effective stress increment ((g) through (i)), and horizontal total stress ((j) through (i)). The first and fourth columns respectively show the distributions of variables on two vertical planes cutting the injection point and the fracture tip, respectively. The second and third columns show the distributions of the variables on two horizontal planes A-A′ (reservoir) and B-B′ (caprock) respectively. The deformation of first and fourth columns is magnified by 500 times.

Unlike the rapid and continuous horizontal propagation, the vertical propagation is slow and contained, since only an absolute height growth of 16 m takes place throughout this stage (Fig. 10 (e) and Fig. 7 (b)). This vertical containment of fracture is mainly because of an amicable

stress gradient. The adopted gradient of S_{hmin} such that $-\mathrm{d}S_{\mathrm{hmin}}/\mathrm{d}z < \rho_c g$ provides a relatively stable condition that halts the upward propagation. This is because it takes more hydraulic head for the caprock fracture to grow at a higher position (Fu et al. 2017).

Fig. 10(e) shows the cooling front in the reservoir rock has advanced a distance equal to approximately a half of the fracture height, nearly 40 m. This results in a significant decrease of total stress perpendicular to the fracture, despite the poromechanical effect that tends to increase the total stress (fig. 10(n)). Meanwhile, the total stress of regions near the fracture front in the caprock is not reduced by the thermo-mechanical effect but rather slightly increases (fig. 10(o)). This stress increase is mostly owing to the additional compression of the caprock to compensate for the cooling contraction of the reservoir. Other studies have also reported this compression of the caprock induced by the injection of cold CO_2 into the reservoir (e.g. Vilarrasa and Laloui, 2015; Salimmda et al. 2017). In this state, the cooling of the reservoir tends to have opposite effects on the total stresses of the reservoir and the caprock. Therefore, the net effect of this discrepancy is that it is much easier to fracture the reservoir rock than the caprock.

Another key observation in this stage is a gradually decreasing injection pressure (Fig. 7(a)). This pressure decrease is owing to the effect of cooling on the total stress of fracture tip region. In the second stage, the fracture tip region, located in the caprock, is largely unaffected by the cooling front (Fig. 9(g)). In this stage, however, the cooling front have traversed the fracture entirely and the near tip region has been cooled, which results in a decrease of total stress (Fig. 10(h) and (p)) and therefore the fracturing pressure decreases.

Note that in all stages analyzed, the propagation of the fracture is still in the leak-off dominated regime and the mass loss introduced by the coupling scheme is marginal, as clearly shown in Fig.8(a). These results demonstrate that the proposed modeling scheme can be employed to effectively simulate the fracture propagation in a leakoff-dominated regime without compromising its accuracy.

Effects of the magnitude of *in situ* stresses in caprock

As reflected in the baseline simulation, the caprock *in situ* stress S_{Cap} plays significant roles in determining the evolution of pumping pressure and affecting the pattern of fracture propagation. However, to what extend the stress difference between S_{Cap} and S_{Rsv} affects the fracture propagation and containment is still unclear. In this section, we evaluate the effects of S_{Cap} on the growth and vertical containment of fluid-driven fractures. Note that $\bar{S}^{C}_{hmin}$ presented in this section denotes the greatest horizontal minimum stresses in the caprock, which is the stress level at the interface with the reservoir.

Fig. 11 show the effects of $\bar{S}^{C}_{hmin}$ (varying from 26 MPa to 32MPa) on fracture propagation and fracture geometries (i.e. fracture heights and lengths). A lower $\bar{S}^{C}_{hmin}$ is as expected to cause a vertically less contained caprock fracturing. Especially in the case with $\bar{S}^{C}_{hmin}$= 26 MPa, the maximum fracture height reach around 192 m, far exceeding the thickness of the reservoir (i.e., 24 m). However, the fracture heights (i.e., 32 and 40 m) in cases with $\bar{S}^{C}_{hmin}$= 30 and 32 MPa are both slightly larger than 24 m and the fracture height (i.e., 88 m) in the baseline locates in between.

Meanwhile, the case with $\bar{S}^{C}_{hmin}$=26MPa where caprock fracturing leads the fracture growth throughout the entire simulation has a long fracture length (i.e. 1053 m after 3 year of CO_2 injection (Fig. 11(a))), whereas the rest of the cases ($\bar{S}^{C}_{hmin}$=28MPa, 30MPa, and 32 MPa) have shorter fracture lengths that are similar to each other (i.e. around 650 m at the end of simulation (Fig. 11(b), (c) and (d))). This discrepancy is caused by the significantly lower leakoff coefficient for the case with $\bar{S}^{C}_{hmin}$=26MPa. First, the difference between the fracture pressure and the pore pressure at far field is lower in the case with $\bar{S}^{C}_{hmin}$=26MPa compared with the other cases for which pumping pressures are quite similar (Fig. 12(a)). This pressure difference drives fluid leakoff from fracture to the reservoir. Second, because in the low caprock stress case caprock fracturing leads the fracturing process, the fracture only penetrates into the reservoir to a short distance, despite the larger overall height. The effective leakoff contact area is only a small fraction of the entire height of the reservoir. The combination of these factors determine that the low stress case has a lower leakoff coefficient and therefore a longer fracture length.

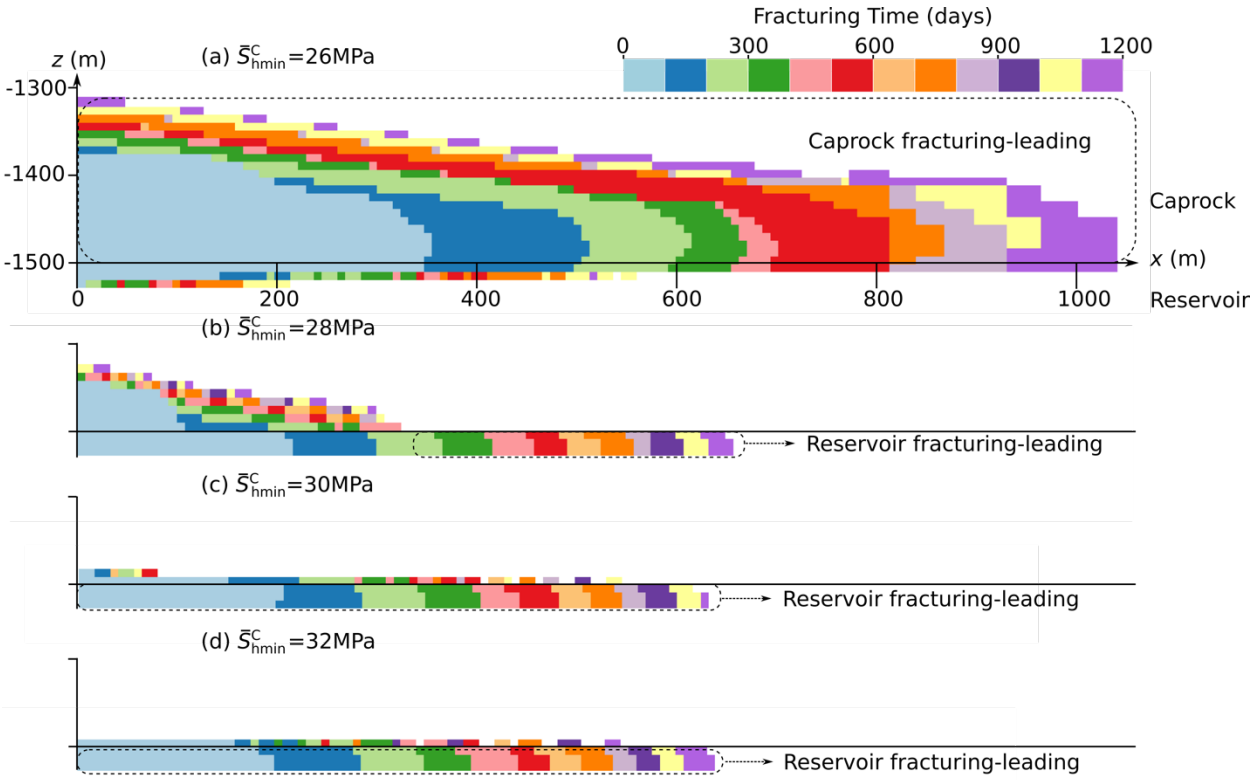

Fig. 11 Effect of the caprock *in situ* stress ((a) 26MPa, (b) 28MPa, (c) 30MPa, and (d) 32MPa on the distribution of fracturing time along the fracture. Quantities are projected onto the the *x*-*z* plane.

The magnitude of $\bar{S}^{C}_{hmin}$ also greatly affects the evolution of injection pressure and maximum aperture (Fig. 12). When $\bar{S}^{C}_{hmin}$ is sufficently high to contain fracturing mostly in the reservoir ($\bar{S}^{C}_{hmin}$=28, 30, 32 MPa), the injection pressure, as disucssed in previous section, experiences first a plateau and then a gradual decline. However, when caprock fracturing leads the overall fracturing throughout the injection ($\bar{S}^{C}_{hmin}$=26 MPa), the injection pressure remains largely constant after fracture grows into the caprock.

Fig. 12(b) shows that maximum apertures in all cases experience continuous increases. Cooling induced by CO_2 injection in the near wellbore region tends to play convoluted roles in affecting maximum apertures under different $\bar{S}^{C}_{hmin}$ levels. For a caprock fracturing-leading case ($\bar{S}^{C}_{hmin}$=26 MPa), the fracture-opening pressure, P^{o}_{f}, near the injection point, owing to the thermal-mechanical effect, could drop significantly. However, the fracture propagation pressure, P_p, which is dictated by the caprock in situ stress near the fracture front, remains largely unchanged (Fig. 12(a)), thereby causing a high net pressure. This high net pressure, in

conjunction with the large overall fracture height, is likely to induce a large fracture aperture in the near-wellbore region. As shown in Fig. 12(b), the maximum aperture in the case with $\bar{S}^{C}_{hmin}$=26MPa reaches around 20 mm. Noticeably, this magnitude of maximum aperture far exceeds the value predicted by isothermal fracture models (McClure and Horne, 2014; Fu et al., 2017). Therefore, employing models that neglects the effects of thermo-elasticity for the simulations of fracturing in GCS tends to underestimate the magnitude of fracture apertures.

For a reservoir fracturing-leading case ($\bar{S}^{C}_{hmin}$=28, 30, 32 MPa), however, the fracture opening pressure and the fracture propagation pressure both tend to decrease (Fig. 12(a)). In other words, there might not be a monotonic increase of net pressure at this region as it is in the case with $\bar{S}^{C}_{hmin}$=26 MPa, which explains a less remarkable increase of aperture magnitude. Meanwhile, the maximum apertures for cases with $\bar{S}^{C}_{hmin}$=30MPa and 32MPa approach to similar values after 300 days of injection. This means in the long run, as long as the caprock stress is high enough to prevent fracture propagation into the caprock, the exact magnitude does not play a significant role in affecting the system response.

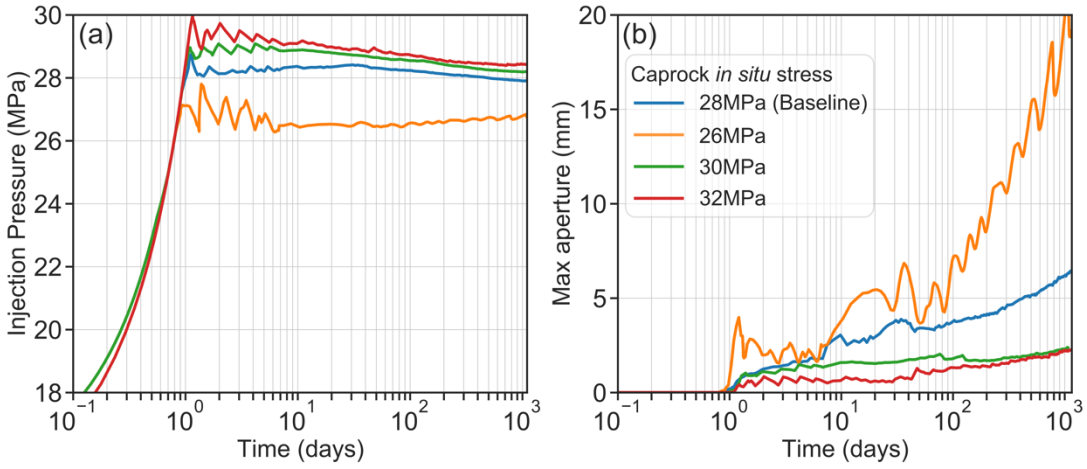

Fig. 12. Effect of the caprock *in situ* stress on (a) the injection pressure and (b) the maximum aperture. The apparent oscilation in the curves is caused by sudden pressure drop when the fracture propagates by the length of an element: a typical artifact for this type of space discretization scheme.

Concluding remarks

This paper develops an efficient and effective modeling scheme for simulating thermo-hydro-mechanical processes in fluid-driven fracturing. Such a modeling capability is crucial for studying geologic carbon storage (GCS) in reservoirs with marginal permeability as in such a scenario, fracture could propagate in both the reservoir and caprock in complex ways. The model captures, in relative high fidelity, multiphase multicomponent fluid flow and heat transfer within fractures and matrix, poro/thermo-mechanical deformation of solid rocks, and fracture propagation. Each of the physical processes is modeled using a robust individual module, and the modules are coupled on a common simulation platform. In order to overcome the numerical challenges posed by coupling many complex processes, we take advantage of some self-stabilizing features of leakoff-dominated fracturing to simplify the numerical coupling. These features enable us to develop a sequential coupling scheme without causing convergence difficulties. Verification against the PKN solution in the leakoff-dominated regime indicates that the simple scheme does not compromise the accuracy of the results for simulating leakoff-dominated fracturing.

In simulating a 3D field-scale injection operation loosely based on the In Salah project, the model reveals complex yet intriguing behaviors of the reservoir-caprock-fluid system. Soon after the injection starts, back-stress caused by pressure diffusion in the reservoir drives a sharp increase in injection pressure to keep the fracture open, until the pressure is high enough to drive fracture propagation in the caprock. The injection pressure then remains largely constant at the caprock's fracturing pressure. Injected fluid continued to be fed into the reservoir through the slowly propagating fracture. Meanwhile, temperature decrease in the reservoir gradually reduces the reservoir's total stress, and eventually the fracturing pressure of the reservoir becomes lower than in the caprock. Thereafter the fracture mainly propagates in the reservoir, and the injection pressure slowly declines accordingly. We also used the model to study the effects of the *in situ* stress contrast between the reservoir and caprock on the vertical containment of the fracture.

We found many processes, including thermal, hydraulic, and mechanical processes, are involved in fracturing caused by CO_2 injection. These processes interact in convolved ways and the relative importance among these processes can evolve as injection progresses. The new model

proves effective in simulating these processes and their complex interactions in fidelity that is unattainable for existing simple models. For example, thermal contraction induced by CO_2 injection has often been speculated to have a negative impact on fracture containment. Our study shows that cold fluid injection itself could actually benefit the geomechanically containment of fracturing under certain stress conditions of caprock. A gradual pumping pressure decline can be used as a practical indicator of fracture growth during injection.

Despite the success in revealing the convoluted interactions among various physical processes, all the simulation in this paper used simple stress profiles. Therefore, a more realistic stress profile with inherent characteristics, such as layered fabrics (Fisher and Warpinski, 2012) and "rough" in situ stress profiles (Fu et al., 2019) considered, should be used to further assess the caprock integrity and system responses in the future.

Acknowledge

This manuscript has been authored by Lawrence Livermore National Security, LLC under Contract No. DE-AC52-07NA2 7344 with the US. Department of Energy. The United States Government retains, and the publisher, by accepting the article for publication, acknowledges that the United States Government retains a non-exclusive, paid-up, irrevocable, world-wide license to publish or reproduce the published form of this manuscript, or allow others to do so, for United States Government purposes.

Reference

Bohloli, B., Ringrose, P., Grande, L., Nazarian, B., 2017. Determination of the fracture pressure from CO_2 injection time-series datasets. Int. J. Greenh. Gas Control 61, 85–93. https://doi.org/10.1016/j.ijggc.2017.03.025

Brooks, R.H., Corey, A.T., 1964. Hydraulic Properties of Porous Media. Hydrology Papers 3. Colorado State University, Fort Collins, CO.

Bunger, A.P., Detournay, E., Garagash, D.I., 2005. Toughness-dominated hydraulic fracture with leak-off. Int. J. Fract. 134, 175–190. https://doi.org/10.1007/s10704-005-0154-0

Eshiet, K.I.I., Sheng, Y., 2014. Carbon dioxide injection and associated hydraulic fracturing of reservoir formations. Environ. Earth Sci. 72, 1011–1024. https://doi.org/10.1007/s12665-013-3018-3

Carrier, B., Granet, S., 2012. Numerical modeling of hydraulic fracture problem in permeable medium using cohesive zone model. Eng. Fract. Mech. 79, 312–328. https://doi.org/10.1016/j.engfracmech.2011.11.012

Coussy, O., 2004. Poromechanics. John Wiley and Sons, Chichester, England.

Culp, D., Tupek, M.R., Newell, P., Hubler, M.H., 2017. Phase-field modeling of fracture in CO_2 sequestration. In: 51st US Rock Mechanics/Geomechanics Symposium. American Rock Mechanics Association ARMA–2017–0644.

Fan, C., Elsworth, D., Li, S., Zhou, L., Yang, Z., Song, Y., 2019. Thermo-hydro-mechanical-chemical couplings controlling CH4 production and CO_2 sequestration in enhanced coalbed methane recovery. Energy 173, 1054–1077. https://doi.org/10.1016/j.energy.2019.02.126

Fu, P., Johnson, S.M., Carrigan, C.R., 2013. An explicitly coupled hydro-geomechanical model for simulating hydraulic fracturing in arbitrary discrete fracture networks. Int. J. Numer. Anal. Methods Geomech. 37, 2278–2300. https://doi.org/10.1002/nag.2135

Fu, P., Settgast, R.R., Hao, Y., Morris, J.P., Ryerson, F.J., 2017. The Influence of Hydraulic Fracturing on Carbon Storage Performance. J. Geophys. Res. Solid Earth 122, 9931–9949. https://doi.org/10.1002/2017JB014942

Fu, P., Huang, J., Settgast, R.R., Morris, J.P., Ryerson, F.J., 2019. Apparent toughness anisotropy induced by “roughness” of in-situ stress: A mechanism that hinders vertical growth of hydraulic fractures and its simplified modeling. SPE J. 24, 2148–2162. https://doi.org/10.2118/194359-PA

Fu, P., Ju, X., Huang, J., Settgast, R. R., Morris, J. P., 2019. THM Modeling of Poroelastic Sustainability of Hydraulic Fracture in CO_2 Storage Reservoirs. In American Rock Mechanics Association. In *Proceedings of the 44th US Rock Mechanics Symposium,* New York, NY, ARMA-2019-1601, 2019.

Fu, P., Ju, X., Huang, J., Settgast, R.R., Liu, F., Morris, J.P., 2020. Thermo-poroelastic responses of a pressure-driven fracture in a carbon storage reservoir and the implications for injectivity and caprock integrity. Int. J. Numer. Anal. Methods. Geomech. 1–19. https://doi.org/10.1002/nag.3165

Francfort, G.A., Bourdin, B., Marigo, J.J., 2008. The variational approach to fracture, Journal of Elasticity. https://doi.org/10.1007/s10659-007-9107-3

Francfort, G.A., Marigo, J.-J., 1998. Revisiting brittle fracture as an energy minimization problem. J. Mech. Phys. Solids 46, 1319–1342. https://doi.org/10.1016/S0022-5096(98)00034-9

Fisher, K., Warpinski, N., 2012. Hydraulic-fracture-height growth: Real data. SPE Prod. Oper. 27, 8–19. https://doi.org/10.2118/145949-pa

Garagash, D.I., Detournay, E., Adachi, J.I., 2011. Multiscale tip asymptotics in hydraulic fracture with leak-off. J. Fluid Mech. 669, 260–297. https://doi.org/10.1017/S002211201000501X

Gheibi, S., Vilarrasa, V., Holt, R.M., 2018. Numerical analysis of mixed-mode rupture propagation of faults in reservoir-caprock system in CO_2 storage. Int. J. Greenh. Gas Control 71, 46–61. https://doi.org/10.1016/j.ijggc.2018.01.004

Girault, V., Kumar, K., Wheeler, M.F., Wheeler, M.F., 2016. Convergence of iterative coupling of geomechanics with flow in a fractured poroelastic medium. Comput. Geosci. 997–1011. https://doi.org/10.1007/s10596-016-9573-4

Guo, B., Tao, Y., Bandilla, K., Celia, M., 2017. Vertically Integrated Dual-porosity and Dual-permeability Models for CO_2 Sequestration in Fractured Geological Formation. Energy Procedia 114, 3343–3352. https://doi.org/10.1016/j.egypro.2017.03.1466

Gor, G.Y., Elliot, T.R., Prevost, J.H., 2013. Effects of thermal stresses on caprock integrity during CO_2 storage. Int. J. Greenh. Gas Control 12, 300–309.

Haszeldine, R.S., 2009. Carbon Capture and Storage: How Green Can Black Be? Science. 325, 1647–1652. https://doi.org/10.1126/science.1172246

Huang, J., Fu, P., Settgast, R.R., Morris, J.P., Ryerson, F.J., 2019. Evaluating a Simple Fracturing Criterion for a Hydraulic Fracture Crossing Stress and Stiffness Contrasts. Rock Mech. Rock Eng. 52, 1657–1670. https://doi.org/10.1007/s00603-018-1679-7

Iding, M., Ringrose, P., 2010. Evaluating the impact of fractures on the performance of the In Salah CO_2 storage site. Int. J. Greenh. Gas Control 4, 242–248. https://doi.org/10.1016/j.ijggc.2009.10.016

International Energy Agency. Energy Technology Perspectives 2010: Scenarios and Strategies to 2050; 2010; International Energy Agency, Paris, France.

Ju, X., Liu, F., Fu, P., D. White, M., R. Settgast, R., P. Morris, J., 2020. Gas Production from Hot Water Circulation through Hydraulic Fractures in Methane Hydrate-Bearing Sediments: THC-Coupled Simulation of Production Mechanisms. Energy & Fuels 0. https://doi.org/10.1021/acs.energyfuels.0c00241

Kim, J., Tchelepi, H.A., Juanes, R., 2011. Stability and convergence of sequential methods for coupled flow and geomechanics: Fixed-stress and fixed-strain splits. Comput. Methods Appl. Mech. Eng. 200, 1591–1606. https://doi.org/10.1016/j.cma.2010.12.022

Kim, J., Moridis, G., Yang, D., Rutqvist, J., 2012. Numerical Studies on Two-Way Coupled Fluid Flow and Geomechanics in Hydrate Deposits. SPE J. 17, 485–501. https://doi.org/10.2118/141304-PA

Kim, J., Moridis, G.J., 2013. Development of the T+M coupled flow-geomechanical simulator to describe fracture propagation and coupled flow-thermal-geomechanical processes in tight/shale gas systems. Comput. Geosci. 60, 184–198. https://doi.org/10.1016/j.cageo.2013.04.023

Howard, G.C., Fast, C., 1957. Optimumfluid characteristics for fracture extension. Drill. Prod. Prac. 24, 261–270.

Li, Z. and Elsworth, D., 2019. Controls of CO_2–N_2 gas flood ratios on enhanced shale gas recovery and ultimate CO_2 sequestration. J. Pet. Sci. Eng. 179, 1037-1045.

Lecampion, B., Bunger, A., Zhang, X., 2018. Numerical methods for hydraulic fracture propagation: A review of recent trends. J. Nat. Gas Sci. Eng. 49, 66–83. https://doi.org/10.1016/j.jngse.2017.10.012

McClure, M.W., Horne, R.N., 2014. An investigation of stimulation mechanisms in Enhanced Geothermal Systems. Int. J. Rock Mech. Min. Sci. 72, 242–260. https://doi.org/10.1016/j.ijrmms.2014.07.011

Mito, S., Xue, Z., Ohsumi, T., 2008. Case study of geochemical reactions at the Nagaoka CO_2 injection site, Japan. Int. J. Greenhouse Gas Control 2, 309–318.

Moridis, G.J., Freeman, C.M., 2014. The RealGas and RealGasH2O options of the TOUGH+ code for the simulation of coupled fluid and heat flow in tight/shale gas systems. Comput. Geosci. 65, 56–71. https://doi.org/10.1016/j.cageo.2013.09.010

Morris, J.P., Hao, Y., Foxall, W., McNab, W., 2011. A study of injection-induced mechanical deformation at the In Salah CO_2 storage project. Int. J. Greenh. Gas Control 5, 270–280. https://doi.org/10.1016/j.ijggc.2010.10.004

Mollaali, M., Ziaei-Rad, V., Shen, Y., 2019. Numerical modeling of CO_2 fracturing by the phase field approach. J. Nat. Gas Sci. Eng. 70, 102905. https://doi.org/10.1016/j.jngse.2019.102905

Nordgren, R.P., 1972. Propagation of a Vertical Hydraulic Fracture. Soc. Pet. Eng. J. 12, 306–314. https://doi.org/10.2118/3009-pa

Orr, F.M., 2009. Onshore geologic storage of CO_2. Science. 325, 1656–1658. https://doi.org/10.1126/science.1175677

Oye, V., Aker, E., Daley, T.M., Kühn, D., Bohloli, B., Korneev, V., 2013. Microseismic monitoring and interpretation of injection data from the In Salah CO_2 storage site (Krechba), Algeria. Energy Procedia 37, 4191–4198. https://doi.org/10.1016/j.egypro.2013.06.321

Pacala, S., Socolow, R, 2004. Stabilization Wedges: Solving the Climate Problem for the Next 50 Years with Current Technologies. Science. 305, 968–972. https://doi.org/10.1126/science.1100103

Paluszny, A., Graham, C.C., Daniels, K.A., Tsaparli, V., Xenias, D., Salimzadeh, S., Whitmarsh, L., Harrington, J.F., Zimmerman, R.W., 2020. Caprock integrity and public perception studies of carbon storage in depleted hydrocarbon reservoirs. Int. J. Greenh. Gas Control 98, 103057. https://doi.org/10.1016/j.ijggc.2020.103057

Pan, L., Oldenburg, C.M., Pruess, K., Wu, Y.-S., 2011. Transient CO_2 leakage and injection in wellbore-reservoir systems for geologic carbon sequestration. Greenh. Gases Sci. Technol. 1, 335–350. https://doi.org/10.1002/ghg.41

Perkins, T.K., Kern, L.R., 1961. Widths of Hydraulic Fractures. J. Pet. Technol. 13, 937–949. https://doi.org/10.2118/89-pa

Raziperchikolaee, S., Alvarado, V., Yin, S., 2013. Effect of hydraulic fracturing on long-term storage of CO_2 in stimulated saline aquifers. Appl. Energy 102, 1091–1104. https://doi.org/10.1016/j.apenergy.2012.06.043

Ren, F., Ma, G., Wang, Y., Fan, L., Zhu, H., 2017. Two-phase flow pipe network method for simulation of CO_2 sequestration in fractured saline aquifers. Int. J. Rock Mech. Min. Sci. 98, 39–53. https://doi.org/10.1016/j.ijrmms.2017.07.010

Rinaldi, A.P., Rutqvist, J., 2013. Modeling of deep fracture zone opening and transient ground surface uplift at KB-502 CO_2 injection well, In Salah, Algeria. Int. J. Greenh. Gas Control 12, 155–167. https://doi.org/10.1016/j.ijggc.2012.10.017

Ringrose, P.S., Mathieson, A.S., Wright, I.W., Selama, F., Hansen, O., Bissell, R., Saoula, N., Midgley, J., 2013. The in salah CO_2 storage project: Lessons learned and knowledge transfer. Energy Procedia 37, 6226–6236. https://doi.org/10.1016/j.egypro.2013.06.551

Rutqvist, J., Vasco, D.W., Myer, L., 2010. Coupled reservoir-geomechanical analysis of CO_2 injection and ground deformations at In Salah, Algeria. Int. J. Greenh. Gas Control 4, 225–230. https://doi.org/10.1016/j.ijggc.2009.10.017

Pruess, K., Tsang, Y.W., 1990. On two-phase relative permeability and capillary pressure of rough-walled rock fractures. Water Resour. Res. 26, 1915–1926. https://doi.org/10.1029/WR026i009p01915

Rutqvist, J., Rinaldi, A.P., Cappa, F., Moridis, G.J., 2013. Modeling of fault reactivation and induced seismicity during hydraulic fracturing of shale-gas reservoirs. J. Pet. Sci. Eng. 107, 31–44. https://doi.org/10.1016/j.petrol.2013.04.023

Salimzadeh, S., Paluszny, A., Zimmerman, R.W., 2017. Three-dimensional poroelastic effects during hydraulic fracturing in permeable rocks. Int. J. Solids Struct. 108, 153–163. https://doi.org/10.1016/j.ijsolstr.2016.12.008

Salimzadeh, S., Paluszny, A., Zimmerman, R.W., 2018. Effect of cold CO_2 injection on fracture apertures and growth. Int. J. Greenh. Gas Control 74, 130–141. https://doi.org/10.1016/j.ijggc.2018.04.013

Salimzadeh, S., Hagerup, E.D., Kadeethum, T., Nick, H.M., 2019. The effect of stress distribution on the shape and direction of hydraulic fractures in layered media. Eng. Fract. Mech. 215, 151–163. https://doi.org/10.1016/j.engfracmech.2019.04.041

Senseny, P.E., Pfeifle, T.W., 1984. Fracture toughness of sandstones and shales. In: The 25th US Symposium on Rock Mechanics (USRMS). 25–27 June, Evanston Illinois.

Settgast, R.R., Fu, P., Walsh, S.D.C., White, J.A., Annavarapu, C., Ryerson, F.J., 2016. A fully coupled method for massively parallel simulation of hydraulically driven fractures in 3-dimensions. Int. J. Numer. Anal. Methods Geomech. https://doi.org/10.1002/nag.2557

Sun, Z., Espinoza, D.N., Balhoff, M.T., 2016. Discrete element modeling of indentation tests to investigate mechanisms of CO_2-related chemomechanical rock alteration. J. Geophys. Res. Solid Earth 121, 7867–7881. https://doi.org/10.1002/2016JB013554

Sun, Z., Espinoza, D.N., Balhoff, M.T., Dewers, T.A., 2017. Discrete Element Modeling of Micro-scratch Tests: Investigation of Mechanisms of CO_2 Alteration in Reservoir Rocks. Rock Mech. Rock Eng. 50, 3337–3348. https://doi.org/10.1007/s00603-017-1306-z

Vilarrasa, V., Olivella, S., Carrera, J., Rutqvist, J., 2014. Long term impacts of cold CO_2 injection on the caprock integrity. Int. J. Greenh. Gas Control 24, 1–13. https://doi.org/10.1016/j.ijggc.2014.02.016

Vilarrasa, V., Laloui, L., 2015. Potential fracture propagation into the caprock induced by cold CO_2 injection in normal faulting stress regimes. Geomech. Energy Environ. 2, 22–31.

Vilarrasa, V., Rinaldi, A.P., Rutqvist, J., 2017. Long-term thermal effects on injectivity evolution during CO_2 storage. Int. J. Greenh. Gas Control 64, 314–322. DOI: 10.1016/j.ijggc.2017.07.019

White, J.A., Chiaramonte, L., Ezzedine, S., Foxall, W., Hao, Y., Ramirez, A., McNab, W., 2014. Geomechanical behavior of the reservoir and caprock system at the In Salah CO_2 storage project. Proc. Natl. Acad. Sci. 111, 8747–8752. https://doi.org/10.1073/pnas.1316465111

White, J.A., Castelletto, N., Tchelepi, H.A., 2016. Block-partitioned solvers for coupled poromechanics: A unified framework. Comput. Methods Appl. Mech. Eng. 303, 55–74. https://doi.org/10.1016/j.cma.2016.01.008

Witherspoon, P.A., Wang, J.S.Y., Iwai, K., Gale, J.E., 1980. Validity of Cubic Law for fluid flow in a deformable rock fracture. Water Resour. Res. 16, 1016–1024. https://doi.org/10.1029/WR016i006p01016

Yan, H., Zhang, J., Zhou, N., Li, M., Suo, Y., 2020. Numerical simulation of dynamic interactions between two cracks originating from adjacent boreholes in the opposite directions

during supercritical CO_2 fracturing coal mass. Eng. Fract. Mech. 223, 106745. https://doi.org/10.1016/j.engfracmech.2019.106745

Van Genuchten, M.T., 1980. A closed-form equation for predicting the hydraulic conductivity of unsaturated soils. Soil Sci. Soc. Am. J. 44 (5), 892–898.